Compact heat exchangers for hydrogen-fueled aero engine intercooling and recuperation

Applied Thermal Engineering 243 (2024) 122538

Contents lists available at ScienceDirect

Applied Thermal Engineering

journal homepage: www.elsevier.com/locate/apthermeng

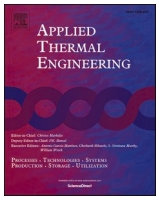

Research Paper

Compact heat exchangers for hydrogen-fueled aero engine intercooling and recuperation

Alexandre Capitao Patrao [a], Isak Jonsson [a], Carlos Xisto [a], Anders Lundbladh [a,b], Tomas Grönstedt [a]

[a] Chalmers University of Technology, Gothenburg SE-41296, Sweden
[b] GKN Aerospace Sweden, Trollhättan SE-46181, Sweden

A B S T R A C T

This study investigates the application of compact heat exchangers for the purpose of intercooling and recuperation systems for short-to-medium range aircraft equipped with hydrogen-fueled turbofan engines. The primary objective is to assess the potential effects of engine-integrated compact heat exchangers on fuel consumption and emissions. The paper encompasses the conceptual design of integrated heat exchangers and associated ducts, followed by aerodynamic optimization studies to identify suitable designs that minimize air-side pressure losses and ensure flow uniformity at the inlet of the high-pressure compressor. Pressure drop correlations are then established for selected duct designs and incorporated into a system-level performance model, allowing for a comparison of their impact on specific fuel consumption, NOx emissions, and fuel burn against an uncooled baseline engine. The intercooled-recuperated engine resulted in the most significant improvement in take-off specific fuel consumption, with a reduction of up to 7.7% compared to the baseline uncooled engine, whereas the best intercooled engine resulted in an improvement of about 4%. Furthermore, the best configuration demonstrated a decrease in NOx emissions by up to 37% at take-off and a reduction in mission fuel burn by 5.5%. These enhancements were attributed to reduced compression work, pre-heating of the hydrogen fuel, and lower high-pressure compressor outlet temperatures.

1. Introduction

The usage of hydrogen as an aviation fuel encompasses several benefits compared to kerosene, including CO2-free combustion, higher gravimetric energy density, and higher cooling capacity. Its principal benefit, combustion without CO2-emissions, makes it an attractive option for decreasing greenhouse gas emissions from aviation and supports the transition to a greener economy. Finding appropriate paths for transition is critical to reach the targets set forth both by ACARE [1] and by the European Union (EU) in the European Green Deal [2] and the more recently by the Fit for 55 policy package [3].

The main challenges for integrating liquid hydrogen propulsion systems into aircraft are connected to the propellant feed system size, mass, and insulation requirements [4], stemming from the relatively low density and cryogenic storage temperatures. Additionally, novel combustion systems are required to address the hydrogen-air mixing and combustion characteristics across different flight regimes and operating conditions [5–8]. Nevertheless, the cryogenic storage temperatures and high heat capacity of liquid hydrogen results in an excellent coolant for an engine heat management system [9–11]. As an example, if hydrogen is used to absorb heat in an aero engine and thereby increase its temperature from tank conditions (24 K) to near core exhaust temperatures (approximately 800 K), then the enthalpy increase will account for approximately 10 % of the fuel lower heating value. In a loss-free system the engine-specific fuel consumption could potentially be reduced by the same amount [12].

Cryogenic hydrogen can be used in an engine heat management system by means of precooling, intercooling, cooled turbine cooling air, and recuperation of exhaust gas heat [9], as exemplified in Fig. 1. In this figure, cryogenic hydrogen flows out of the tank, being first pressurized by a booster pump and subsequently by an inline pump to increase the pressure above its critical value. It then flows towards the engine, where it will experience one final pressurization by the high-pressure engine mounted pump. Afterwards, it flows through a guide vane or heat exchanger positioned at the low-pressure compressor (LPC) inlet where it pre-cools the fan-discharge core air [9–11,13,14]. Thereafter, the hydrogen flows through a heat exchanger positioned in the intermediate compressor duct (ICD), located between the LPC and high-pressure compressor (HPC), to cool the LPC discharge air, which is normally denoted as intercooling, a concept which has been studied previously [12,15–17]. Precooling and intercooling will exchange heat from the engine core to the fuel, hence increasing the fuel enthalpy, decreasing the required compression work [18], and for a fixed overall pressure ratio (OPR) decreasing NO_x emissions [19–21]. One possible challenge with the configuration shown in Fig. 1, is connected to the cryogenic fuel temperatures and the presence of humid air. If the air-side temperature is below water freezing levels, this might cause a partial or complete blockage of the engine core air flow. This hazard is more critical in the precooler due to the lower temperatures expected at the engine core inlet [22].

An alternative to integrating a separate intercooler heat-exchanger component, is using existing turbomachinery surfaces to perform

https://doi.org/10.1016/j.applthermaleng.2024.122538
Received 30 November 2023; Received in revised form 16 January 2024; Accepted 23 January 2024
Available online 28 January 2024

Nomenclature

A	Area [m^2]
ACARE	Advisory Council for Aviation Research and Innovation in Europe
AR	Area ratio
BPR	Bypass ratio
C	Flow capacity rate [W/K]
CAS	Calibrated airspeed
c_p	Specific heat capacity [J/kg K]
D_h	Hydraulic diameter [m]
DP	Design Point
DT_ISA	Temperature offset for the ISA [K]
EINOx	Emission index of NO_x [g/kg]
f	Friction factor
FB	Fuel burn
FPR	Fan pressure ratio
G	Mass flux [kg/m^2 s]
GA	Genetic Algorithm
GESTPAN	General Stationary and Transient Propulsion Analysis tool
GHG	Greenhouse gas
h	Enthalpy [J/kg K]
h_{air}	Air-side convective heat transfer coefficient [W/m^2 K]
h_{H2}	H_2-side convective heat transfer coefficient [W/m^2 K]
H_{blade}	Blade height [mm]
HEX	Heat Exchanger
HPC	High-Pressure Compressor
HPT	High-Pressure Turbine
ICD	Intermediate compressor duct
ISA	International Standard Atmosphere
j	Colburn j-factor
k	Thermal conductivity [W/m K]
K	Pressure loss coefficient
L_{fin}	Fin length [m]
L_{long}	Longitudinal spacing between heat exchanger tubes [m]
L_{trans}	Transversal spacing between heat exchanger tubes [m]
L_x	HEX length in air direction [m]
L_y	HEX length in H_2 direction [m]
L_z	HEX length in circumferential direction [m]
LHS	Latin Hypercube Sampling
LPC	Low-Pressure Compressor
LPT	Low-Pressure Turbine
M	Mach number
$\dot{m}$	Mass flow [kg/s]
N_{banks}	Number of tube banks
N_{fins}	Number of heat exchanger fins
N_{passes}	Number of heat exchanger passes
N_{tubes}	Number of heat exchanger tubes
N_{TU}	Number of Transfer Units
NO_x	Nitrous oxides
Nu	Nusselt number
OPR	Overall Pressure Ratio
p	Pressure [Pa]
p_3	HPC outlet pressure [Pa]
P	Perimeter [m]
PAX	Passengers
P_i	Bézier curve control point i
Pr	Prandtl number
PVC	Polyvinyl chloride plastic
Q	Heat flow [W]
q	Volumetric heat source [W/m^3]
r	Radius from engine rotational axis [m]
r_{ICD}	Radial distance in local ICD coordinate system [m]
R	Radius [m]
RBF	Radial Basis Functions
RC	Recirculation factor
Re	Reynolds number
s_{fin}	Fin spacing [m]
SFC	Specific Fuel Consumption
SMR	Short-to-Medium Range
St	Stanton number
t_{tube}	Tube thickness [m]
T	Temperature
T_3	HPC outlet temperature [K]
T_{31}	Combustor inlet temperature [K]
T_4	Combustor outlet temperature [K]
T_{fuel}	Fuel temperature at injector [K]
TO	Take-off
ToC	Top-of-climb
TRS	Turbine Rear Structure
U	Overall heat transfer coefficient [W/m^2 K]
v	Velocity [m/s]
v_{18}	Cold nozzle exhaust velocity [m/s]
v_8	Hot nozzle exhaust velocity [m/s]
v'	Velocity perturbation at the HEX inlet [m/s]
V_{HEX}	Heat Exchanger total volume [m^3]
V_{trans}	Transversal velocity at HEX inlet [m/s]
W	Mass [kg]
W_{pump}	Pumping power [W]
WEICO	Weight and Cost tool
x	Longitudinal distance from the fan face [m]
x_{ICD}	Axial distance in local ICD coordinate system [m]
y^+	Mesh first wall node height

Greek letter symbols

α_{air}	Total air-side transfer area/total volume [1/m]
α_{H2}	Total H_2-side transfer area/total volume [1/m]
β	Hub and casing wall angle
$\Delta_{FB.total}$	Fuel burn variation due to variations in engine weight and SFC
$\Delta R/L$	Shape factor of the ICD
δ_{fin}	Fin thickness [m]
ϵ	Heat exchanger effectiveness
η_0	Overall air-side surface effectiveness
η_{fin}	Fin effectiveness
η_p	Polytropic efficiency
γ	Ratio of specific heat capacities
κ_{fin}	Fin area/total area
λ	Inertial resistance factor [1/m]
μ	Dynamic viscosity [Pa s]
Π	Correction factor for polytropic efficiency
ϕ	Combustion chamber equivalence ratio
ψ	Flow non-uniformity
ρ	Density [kg/m^3]
σ_{air}	Free-flow area/frontal area
θ	Temperature difference for heat transfer [K]

direct cooling of the core air. This approach could potentially provide the largest performance improvements, since it accomplishes the heat transfer without adding new surfaces into the flow. However, a number of challenges arise from this approach, primarily connected to the integration of small pressurized channels into aerodynamically designed turbomachinery parts [20,23,24]. The study conducted by Dijk et al [24] explored the use of existing turbomachinery surfaces for heat transfer, focusing on integrating the coolant channels in the stator base, allowing the stator to act as a fin. Dijk et al also studied the integration of a single coolant loop within the stator blades and arrived at the conclusion that the heat transfer was limited by the surface area on the hydrogen cooling channel. This concept was further developed by the authors of the present paper by analyzing the heat transfer performance of the LPC stator vanes [19]. The vanes were designed to contain an internal cooling circuit composed of numerous small cooling channels adjacent to the outer vane surface, thereby increasing the hydrogen-side heat transfer area. This cooling concept showed that it was possible to achieve high heat transfer rates, but the cycle performance improvements in terms of SFC and NOx emissions were constrained by the limited amount of the air-side surface area of the LPC stator vanes.

As shown in Fig. 1, the hydrogen flowing out from the intercooler can be used to cool the turbine cooling air, thereby decreasing the required turbine cooling air mass flow [25,26]. Afterwards, the hydrogen flows into the recuperator at the rear of the engine and recovers the thermal energy available at the exhaust, transferring it back into the engine. Recuperation could also be carried out through cooling with core air from the HPC [27–31], but requires larger heat exchangers since both working fluids are mainly composed of air. Ito and Nagasaki [32] investigated an intercooled-recuperated engine, using two separate closed fluid loops. One loop absorbed heat directly by integrating cooling into the stators and then ejecting it into the bypass stream. A second loop was used to recuperate heat from the turbine exhaust and transfer it into the core air stream at the last stages of the HPC. For this configuration, system level simulations showed an estimated SFC reduction of 6 %.

It is noted that the arrangement in Fig. 1 is only illustrative. An optimal architecture would be subjected to a detailed assessment of the integrated performance, including safety and operability aspects at design and off-design conditions. For the purpose of this paper the engine configuration will be simplified to only feature intercooling and recuperation. Hydrogen will be assumed to flow directly from the engine pump to the intercooler. From the intercooler it will either be injected into the combustion chamber or pass through the recuperator to pick up the exhaust heat before reaching the combustion chamber.

Whether for intercooling or recuperation, the main difficulties in designing highly effective heat transfer components for aero engines reside in achieving high heat transfer rates while minimizing pressure losses and weight. For this purpose, a new type of compact heat exchanger is presented in this paper which is suitable for integration in the intermediate compressor S-duct, between the LPC and HPC in Fig. 1, for the purpose of intercooling. The main function of the duct is to diffuse the flow to decrease its dynamic pressure prior to entering the heat exchanger, where it then exchanges heat with the fuel. The proposed design is a compact solution, suitable for aero-engine integration that enables high heat transfer rates with low to moderate pressure drops. This type of design allows the intercooler to be integrated into the gas path, without ducting the core air to a separate cooling stream as previously suggested by [33–37]. Moreover, the increased heat capacity of hydrogen allows for a more compact system, achieving higher heat transfer rates, hence minimizing weight and volume. At the same time, the proposed solution does not require the usage of fan discharge air as a heat-sink, as proposed in [33–37], removing the need of auxiliary ducts as well as avoiding the increased pressure drop on the external air-side of the heat exchanger. These outlined characteristics, associated with the thermal benefits of increasing the fuel energy content with intercooling and recuperation, should lead to improved component-based heat-transfer and overall thermal conversion performance, which will be addressed in the present paper.

The integrated performance of compact heat exchangers is expected to be of great importance in future cryogenic hydrogen powered aircraft engines. The integrated aspects include the aerodynamic performance of the connecting ducts, which have a direct impact on the engine thermal efficiency, as well as the associated weight and volume which mainly impacts aircraft performance. These aspects have been only rudimentarily modeled [24] or assumed negligible [12,20,21,23] in earlier studies. Clearly, a more in-depth multi-level analysis of the design, performance, and impact of compact heat exchangers on hydrogen aero engines is required. This paper addresses this gap by providing a systematic approach to the design and performance of integrated hydrogen heat exchangers. It includes heat exchanger conceptual design, component aerothermal performance and optimization, detailed flow analysis, engine system level simulations, and impact on flight mission fuel burn and emissions. This multi-level analysis will enable more accurate estimates of engine performance and fuel burn, especially considering the heat exchanger air-side pressure losses and installation weight, both of which have an impact on hydrogen aircraft performance. To the best

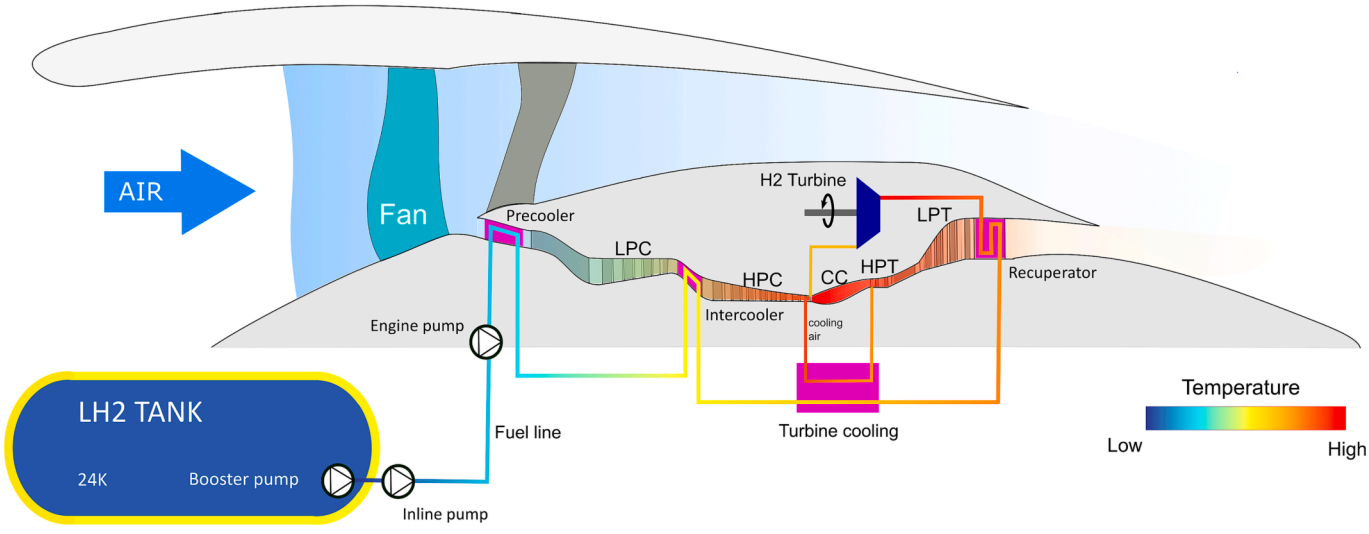

Fig. 1. Example of a heat management system for a turbofan engine featuring precooling, intercooling, recuperation, and cooled turbine cooling air.

knowledge of the authors, this paper represents the first attempt at such a multi-level analysis of heat exchangers in hydrogen aero engines.

The outline of this work is as follows; in section 2 a design framework is established for the conceptual design of compact cryogenic heat-exchangers. The tool is informed by preliminary engine thermodynamic and conceptual design studies that determine the operating conditions, boundary conditions, and ICD corner points, hence defining the design space of the heat-exchanger and associated ducts. In Section 3.1 the heat exchanger conceptual design is carried out using the method described in Section 2.1. An aerodynamic optimization campaign follows in Section 3.3 to address the design and performance of the ICD ducts by means of CFD simulations, following the methodology presented in Section 2.2. Pressure drop correlations are then generated and presented in Section 3.5 for the chosen integrated duct and heat exchanger designs. These correlations are fed back into a system level model (described in Section 2.3) to assess the impact of intercooling and recuperation on overall engine performance and engine conceptual design. The system level performance is evaluated in Sections 3.7 And 3.8 in terms of SFC, mission fuel burn, and NO_x emissions.

2. Methodology

The overall methodology used in the paper is shown in Fig. 2. First, a baseline engine configuration is defined. This engine excludes cooling but provides the aerothermal boundary conditions and ICD corner points needed for the heat exchanger conceptual design. The output from this step consists of heat exchanger size, heat flow, and estimating the heat exchanger matrix pressure drop, which is fed into the duct shape optimization studies, which in turn optimizes the geometry of the ICD duct. Pressure loss correlations are then obtained for a set of optimized ducts which are then included in the engine system level performance calculations. Ideally, this last step would feed back to the heat exchanger conceptual design for an additional design update loop, but for this paper the process is run linearly between step 1 and 4, with only a few minor alterations carried out for the heat exchanger design parameters between step 3 and 4.

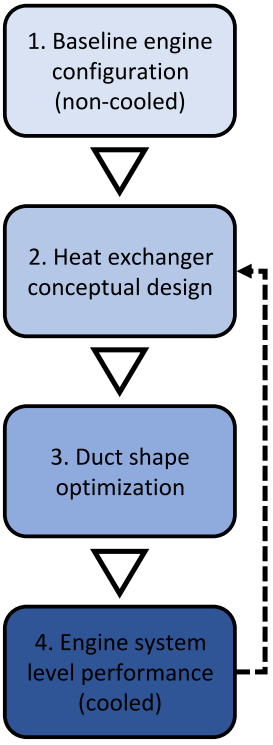

Fig. 2. An outline of the overall methodology for the paper.

The structure of this section will not exactly follow the sequence in Fig. 2 since the first and last steps employ the same methodology. Instead, this section begins with a description of the approach used for conceptual design of the compact heat exchangers, covering the type of heat exchanger used, design parameters, and how its aerothermal performance is calculated. It is followed by a section describing the design and optimization process used for generating low loss duct designs integrated with the aforementioned heat exchangers. The last part of the methodology section covers the engine system level model used to assess the impact of the compact heat exchangers on engine performance.

2.1. Heat exchanger conceptual design

The aim of a heat exchanger design is to transfer as much heat as possible while minimizing the incurred pressure drops for the working fluids. For an air-to-liquid heat exchanger this usually means designing for a low Mach number for the air flowing through the heat exchanger. This was shown by Wilson [38], who used Reynolds' analogy to derive an expression for the ratio between available heat flow Q in a heat exchanger with the required pumping power W_{pump} needed to overcome the pressure losses in the air stream:

$$\frac{Q}{W_{pump}} = \frac{\theta/T}{M^2(\gamma - 1)} \tag{1}$$

Here, θ represents the temperature difference driving the heat flow Q while M represents the Mach number. In essence, this expression highlights the importance of reducing the Mach number of the flow to increase heat transfer to pumping power ratio. One approach for avoiding excessive air-side pressure losses is to first diffuse the flow to decrease its dynamic pressure before cooling it in a heat exchanger. An example of this setup is provided in Fig. 3, which shows a heat exchanger integrated with an ICD and which is compatible with the LPC outlet and HPC inlet radii. The air flows from left to right, first through a diffuser duct, then a conical heat exchanger (HEX), followed by a contraction which accelerates the flow towards HPC. The area ratio (AR) between the diffuser duct inlet and outlet dictates which Mach number can be obtained at the heat exchanger face, as shown in Table 1, assuming a well-functioning diffusor with low losses and without flow separation. The diffuser inlet Mach number of 0.4 used here is typical for the LPC outflow on existing engines [39,40].

The type of heat exchanger geometry chosen for this study needs to allow for high amounts of heat transfer while minimizing the air-side pressure drop. Various types of heat exchanger matrices from Kays and London [41] were considered, including in-line tube banks, staggered tube banks, finned circular tubes, and flattened tubes. The chosen matrix, a finned flat tube type heat exchanger with the designation 9.1–0.737-S, is illustrated in Fig. 4. Here, it is assumed that core air flows between the fins while hydrogen flows inside the pipes featuring the stadium-shaped cross-section. This geometry was chosen primarily due to the inclusion of the fins, the tube cross-section, and the staggered configuration. The fins not only increase the overall surface area but also provide structural support for the tubes and help guide the flow when included in an ICD such as the one presented in Fig. 3. The tube cross-section is more aerodynamically streamlined than corresponding circular cross-sections, while the staggered configuration leads to new boundary layer formation at each tube leading edge – thereby increasing local heat transfer. As shown in Table 2, this geometry provides a relatively large heat transfer surface area to heat exchanger volume ratio (α_{air}) and a high ratio of free-flow area versus frontal area (σ_{air}), both of which are beneficial in terms of heat transfer and pressure drop. It should be noted that the heat exchanger matrix has not been analyzed in terms of strength and durability. Neither has any refinement or optimization of the matrix geometry been carried out.

Pressure drop and heat transfer correlations for this heat exchanger geometry are provided by Kays and London [41] in terms of plots of the

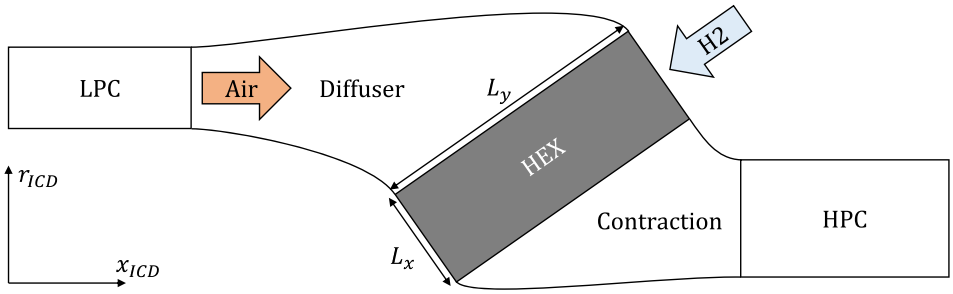

Fig. 3. Meridional view of an integrated ICD duct and HEX. L_x constitutes the length of the HEX in the air direction and L_y in the direction of the hydrogen flow. There is also a circumferential length L_z (not shown) which intersects the centroid of the HEX.

Table 1
Ideal diffuser outlet Mach number for a series of area ratios (AR).

Inlet Mach number	AR	Ideal outlet Mach
0.4	1	0.400
	2	0.186
	4	0.091
	6	0.061
	8	0.046
	10	0.036

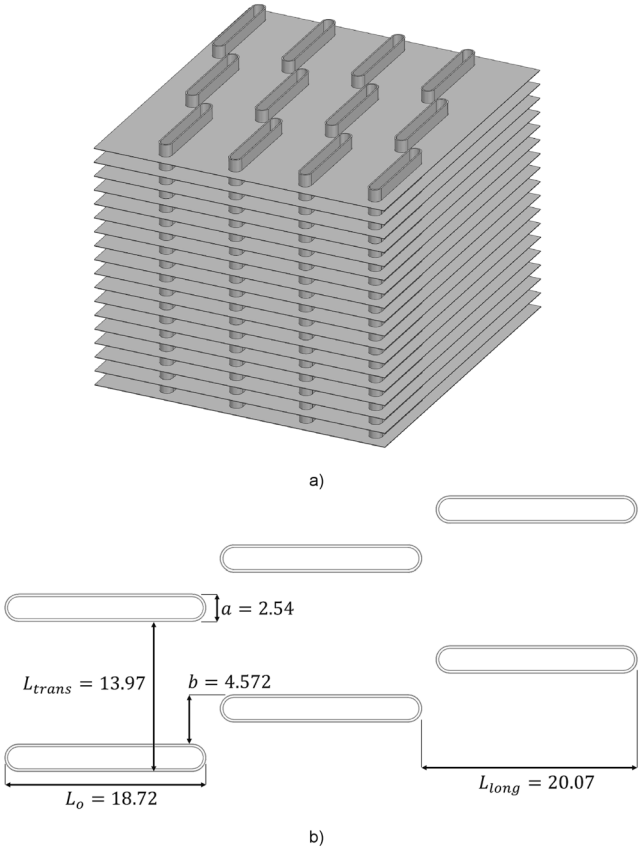

Fig. 4. (a) 3d representation of the 9.1–0.737-S finned flat tube heat exchanger geometry. In this image it features three banks of tubes (N_{banks}). (b) Cross-sectional view of the heat exchanger tube and their relative position to each other (units in millimeters).

Colburn *j*-factor ($j = StPr^{2/3}$) and friction factor f as function of Reynolds number. These have been digitized and are used for calculating the heat exchanger performance using the $\epsilon - N_{TU}$ method, which is described in the next section.

Table 2
Heat exchanger 9.1–0.737-S design properties.

Parameter	Value
Free-flow area/frontal area σ_{air}	0.788
Fin area/total area κ_{fin}	0.813
Fin spacing s_{fin} [mm]	2.794
Fin thickness [mm]	0.1
Total air-side transfer area/total volume $\alpha_{air}\,[m^2/m^3]$	734.9
Tube wall thickness t_{tube} [mm]	0.254
Air-side hydraulic diameter $D_h[mm]$	4.206

2.1.1. The ε-NTU method

The $\epsilon - N_{TU}$ method [41,42] has been implemented in an in-house Python code for calculating the heat exchanger performance. A step-by-step description of the calculation procedure will be provided in subsequent sections.

Step 1 - Defining dimensions

The conical heat exchanger in Fig. 3 is treated as a rectangular box with dimensions according to Fig. 5 for the purpose of the calculations performed here, thereby preserving the volume, cross-sectional area, and cross-sectional dimensions. The dimensions of the heat exchanger are used to calculate the total heat exchanger volume V_{HEX}:

$$V_{HEX} = L_x L_y L_z \tag{2}$$

At this stage, initial estimates for the heat exchanger effectiveness ϵ and pressure drops are set, which allows for an estimation of the outlet conditions of the heat exchanger. In this subsection of the paper HEX inlet conditions are denoted by subscript 1 and outlet conditions by subscript 2. The effectiveness on the air-side of the heat-exchanger is defined as:

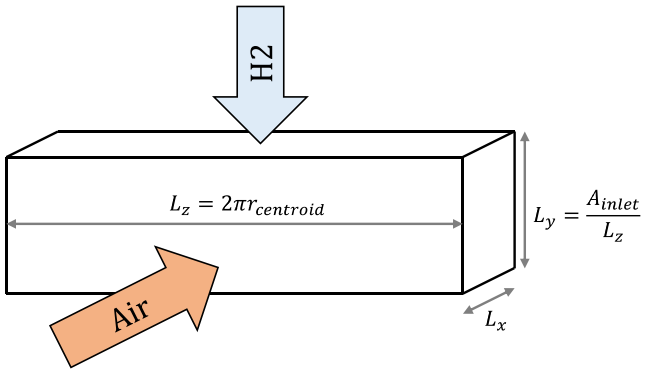

Fig. 5. Dimensions of the heat exchanger used for conceptual design. $r_{centroid}$ refers to the radius of the centroid of the HEX in Fig. 3.

$$\epsilon = \frac{C_{air}\left(T_{air,1} - T_{air,2}\right)}{C_{min}\left(T_{air,1} - T_{H2,1}\right)} \tag{3}$$

where the minimum, air side and hydrogen flow capacity rates are given by:

$$\begin{aligned} C_{\min} &= min(C_{air}, C_{H2}) \\ C_{air} &= \bar{c}_{p,air}\dot{m}_{air} \\ C_{H2} &= \bar{c}_{p,H2}\dot{m}_{H2} \end{aligned} \tag{4}$$

Re-arranging Eq. (3) yields the outlet temperature for the air side:

$$T_{air,2} = T_{air,1} - \epsilon\left(\frac{C_{min}}{C_{air}}\right)\left(T_{air,1} - T_{H2,1}\right) \tag{5}$$

The hydrogen outlet temperature is obtained through conservation of energy:

$$T_{H2,2} = T_{H2,1} + \left(\frac{C_{air}}{C_{H2}}\right)\left(T_{air,1} - T_{air,2}\right) \tag{6}$$

This allows for calculating average thermophysical properties (e.g. thermal conductivity $\bar{k}$ and viscosity $\bar{\mu}$) of the fluids. They are evaluated at the arithmetic average of the temperatures and pressures at corresponding inlets and outlets for each fluid. The average specific heat capacities $\bar{c}_p$ are calculated using the inlet and outlet conditions for each fluid as follows:

$$\bar{c}_p = \frac{h_2 - h_1}{T_2 - T_1} \tag{7}$$

Step 2 - Calculating friction factors and heat transfer coefficients

The heat transfer coefficients and friction factors can be calculated using the overall dimensions of the heat exchanger and the inlet conditions for the hydrogen and air sides. First, the air side frontal area can be calculated:

$$A_{front,air} = L_z L_y \tag{8}$$

whereas the mass flux,

$$G_{air} = \frac{\dot{m}_{air}}{\sigma_{air} A_{front,air}}, \tag{9}$$

can be estimated for a given heat-exchanger geometry, where σ_{air} is the freeflow area to frontal area ratio (Table 2) of the air side. The Reynolds number on the air side can now be calculated:

$$Re_{air} = \frac{D_{h,air} G_{air}}{\bar{\mu}_{air}} \tag{10}$$

where $D_{h,air}$ is the hydraulic diameter and $\bar{\mu}_{air}$ is the average dynamic viscosity. The Reynolds number allows for the estimation of the friction f, and Colburn factor j using the available empirical correlations which in turn allow for calculating the air-side heat-transfer performance:

$$Nu_{air} = RePr^{1/3} j \tag{11}$$

$$h_{air} = \frac{Nu_{air}\bar{k}_{air}}{D_{h,air}} \tag{12}$$

Regarding the hydrogen side, the frontal area, mass flux and Reynolds number are calculated as follows:

$$A_{front,H2} = L_z L_x \tag{13}$$

$$G_{H2} = \frac{\dot{m}_{H2}}{\sigma_{H2} A_{front,H2}} \tag{14}$$

$$Re_{H2} = \frac{D_{h,H2} G_{H2}}{\bar{\mu}_{H2}} \tag{15}$$

The free-flow factor, σ_{H2} is calculated using the dimensions in Fig. 4, as is the hydraulic diameter. The friction factor f and the Nusselt number on the hydrogen side are calculated using correlations by Petukhov [43] and Gnielinski [44], as shown in Eqs. (16) and (17), respectively. For laminar flow ($Re < 3000$) the friction factor is calculated as $f = 64/Re_{H2}$ and the Nusselt number as 3.66.

$$f = (0.79\ln Re_{H2} - 1.64)^{-2} \text{ for } Re_{H2} \geq 3000 \tag{16}$$

$$Nu_{H2} = \frac{(f/8)(Re_{H2} - 1000)Pr_{H2}}{1 + 12.7(f/8)^{1/2}(Pr^{2/3} - 1)} \tag{17}$$

$$h_{LH2} = \frac{Nu_{H2} \bullet \bar{k}_{H2}}{D_{h,H2}} \tag{18}$$

The Reynolds and Prandtl numbers are expected to be within the range of applicability for the given correlations ($0.5 < Pr < 2000$ and $Re < 5 \times 10^6$).

Step 3 - Calculating fin and overall surface effectiveness

The fin effectiveness is calculated as shown below:

$$\eta_{fin} = \frac{\tanh\left(mL_{fin}\right)}{mL_{fin}} m = \sqrt{\frac{2h_{air}}{k_{fin}\delta_{fin}}} \tag{19}$$

where L_{fin}, k_{fin}, δ_{fin} is the fin length, thermal conductivity, and thickness, respectively. Next the overall surface effectiveness of the air side can be calculated using the ratio of fin area to total area κ_{fin}:

$$\eta_0 = 1 - \kappa_{fin}\left(1 - \eta_{fin}\right) \tag{20}$$

Step 4 - Calculating HEX effectiveness

First, the air-side overall heat transfer coefficient U_{air} is calculated using the Eq. (21):

$$\frac{1}{U_{air}} = \frac{1}{\eta_0 h_{air}} + \frac{1}{\left(\frac{\alpha_{H2}}{\alpha_{air}}\right) h_{H2}} \tag{21}$$

Here it is assumed that the wall thermal resistance can be neglected (due to thin tube walls) and that the heat transfer surfaces are clean, i.e.no fouling. Likewise, longitudinal heat transfer along the heat exchanger tubes and fins has also been neglected since it is estimated to amount to less than 1 % of the overall heat flow. The ratio between air-side transfer area to volume, α_{air}, is included in Table 2, while α_{H2} is calculated using the tube perimeter P_{tube} and tube frontal area:

$$\alpha_{H2} = \frac{P_{tube}}{\left(L_{trans} L_{long}\right)} \tag{22}$$

where L_{trans} is the transversal spacing and L_{long} is the longitudinal spacing between each tube (see Fig. 4). The number of transfer units N_{tu} can now be calculated:

$$N_{tu} = \frac{V_{HEX}\alpha_{air}U_{air}}{C_{min}} \tag{23}$$

The effectiveness of the heat exchanger can now be obtained from Eq. (24) which is applicable for an unmixed crossflow heat exchanger:

$$\epsilon = 1 - \exp\left[\left(\frac{C_{max}}{C_{min}}\right) N_{TU}^{0.22}\left(\exp\left(-\frac{C_{min}}{C_{max}} N_{TU}^{0.78}\right) - 1\right)\right] \tag{24}$$

The outlet temperature for the air and hydrogen sides is readily obtained with Eqs. (5) and (6) and the overall heat flow is calculated as follows:

$$Q = C_{air}\left(T_{air,1} - T_{air,2}\right) \tag{25}$$

The air-side pressure drop is calculated according to Kays [41]:

$$\Delta p_{air} = \frac{G_{air}^2}{2\rho_{air,1}}\left(\left(1+\sigma_{air}^2\right)\left(\frac{\rho_{air,1}}{\rho_{air,2}} - 1\right) + f\frac{4L_x}{D_{h,air}}\frac{\rho_{air,1}}{\overline{\rho}_{air}}\right) \tag{26}$$

where $\overline{\rho}_{air} = 0.5\left(\rho_{air,1} + \rho_{air,2}\right)$ is the average air density on the air-side. The pressure drop on the hydrogen side is calculated using the Darcy–Weisbach equation re-written in terms of mass-flux.

$$\Delta p_{H2} = 2\frac{G_{H2}^2}{\overline{\rho}_{H2}} f \frac{L_y}{D_{h,H2}} \tag{27}$$

At this stage, step 1 is updated using the new outlet conditions and subsequent steps repeated. This is particularly important when the heat exchanger working fluids are treated as real fluids or gases whose thermophysical properties vary with temperature and pressure. The steps outlined in this section can be iterated to reach desired accuracy, e.g. with respect to pressure loss or resulting heat exchanger effectiveness.

Recirculating hydrogen from the outlet of the heat exchanger and mixing it with incoming cold hydrogen is used as a strategy for controlling the hydrogen inlet temperature to the tubes of the HEX. This is done by carrying out additional iterations of the $\epsilon - NTU$ method where the hydrogen inlet temperature is updated using the total enthalpy at the outlet of the HEX ($h_{H2,02}$) and the recirculation factor *RC*:

$$RC = \frac{\dot{m}_{H2,recirc}}{\dot{m}_{H2}} \tag{28}$$

$$h_{H2,0,mixer} = \frac{h_{01} + RC \bullet h_{H2,02}}{1 + RC} \tag{29}$$

2.1.2. Thermophysical properties

The thermophysical properties used in heat exchanger conceptual design are obtained from the National Institute of Standards and Technology (NIST) *Reference Fluid Thermodynamic and Transport Properties Database* (REFPROP) [45] via the Python wrapper for CoolProp [46]. This provides easy access to highly accurate real fluid/gas properties for the conceptual design process. For these calculations a dry air mixture has been chosen for the air side of the heat exchanger. Later, for the system level recuperation design and performance studies, discussed in section 3.7.2, tabulated data will be used to calculate the air side gas properties resulting from the combustion of the hydrogen-air mixture.

Hydrogen exists in two different isomers, ortho- and parahydrogen, depending on the orientation of the nuclear spin of the atoms in the hydrogen molecule. The equilibrium distribution of the two isomers varies with temperature, with a sample kept at 19 K having a 99.75 % parahydrogen content, which converts to orthohydrogen with increasing temperature until a 75 % ortho- and 25 % parahydrogen mixture is obtained at room temperature. This mixture is commonly referred to as normal hydrogen and its distribution is constant for higher temperatures [47]. Obtaining liquid hydrogen requires liquification (cooling) to temperatures below the boiling point of hydrogen (20.3 K at atmospheric pressure), which will convert the majority of the hydrogen molecules to its para isomer, a process which can take days to reach equilibrium conditions [47,48]. This can be reduced to minutes by employing a catalyst such as iron oxide (Fe_2O_3) or chromium oxide (CrO) [49,50]. This paper assumes that the hydrogen used in the aircraft has been stored at cryogenic temperatures for several days or has undergone catalytic conversion to, in essence, pure parahydrogen. This also has an advantageous impact on heat transfer since one of the major differences between the two isomers is the higher specific heat capacity c_p of parahydrogen, which is almost 40 % higher than orthohydrogen (at 140 K), making it the better coolant. Furthermore, it is assumed that the hydrogen remains in its para state throughout the heat transfer process since the timescale of the conversion process is in the order of hours, even at room temperature [51].

2.2. Duct shape optimization

For the heat exchanger to operate under optimal conditions the diffuser duct needs to uniformly diffuse the flow while minimizing the incurred pressure losses. Flow uniformity in the heat exchanger inlet minimizes the internal heat exchanger pressure loss and avoids non-uniform cooling which can lead to cold streaks. Downstream of the heat exchanger the flow is then guided by a contraction duct towards the HPC inlet, while keeping the pressure loss to a minimum. This essentially defines the optimization problem as follows:

- Minimize the sum of the total pressure losses in the diffuser and the contraction.
- Minimize the non-uniformity ψ of the velocity at the inlet of the heat exchanger (diffuser outlet):

$$\psi = \int_{A_{inlet}} \frac{1}{2} v'^2 dA \Big/ \int_{A_{inlet}} \frac{1}{2} V^2 dA \tag{30}$$

The flow perturbation v' on the heat exchanger inlet is defined as the difference between the velocity at a specific point, V, and the averaged velocity on the HEX inlet surface (see Fig. 3).

$$v' = V - \frac{1}{A_{inlet}} \int_{A_{inlet}} V dA \tag{31}$$

In essence, minimizing ψ minimizes the kinetic energy in the flow perturbation v'. An additional objective function was included to minimize the surface area of the ducts, leading to decreased volume and mass.

The optimization process is described in Fig. 6 and is based on the Chalmers in-house optimization platform described in [52–54]. It starts by generating an initial set of designs by means of a Latin Hypercube Sampling (LHS) of the design space. The design variables consist of the axial and radial position of the HEX centroid, its inclination, and control points for defining the Bézier curves for the diffuser and contraction ducts, as shown in Fig. 7. The control points of the Bézier curves have been constrained in order to match the slopes of connecting hub and shroud curves, e.g. for curve C2 where points P_8 and P_2 form a line parallel with curve C11 or points P_3 and P_F which form a line parallel with curve C16.

The next step consists of mesh generation, which is carried out using the software Pointwise. The resulting mesh is unstructured (Fig. 8) with quadratic elements along the hub and shroud walls and a mixture of triangular and quadrilateral elements in the rest of the domain. A first wall node height of 10^{-6} m is used to obtain an average y^+ well below 1. Cell counts vary for the different designs generated during the optimization, usually fluctuating around 50 k-150 k cells. Mesh refinement is carried out at a later stage in this paper for selected designs from the optimization campaign in order to generate pressure loss correlations.

Two-dimensional, axisymmetric, steady-state CFD simulations are then carried out for all the designs using the commercial solver ANSYS Fluent 2021 R1, commonly used to model complex engineering applications such as heat exchangers [55]. The compressible Reynolds Averaged Navier-Stokes (RANS) equations are solved together with the $k - \omega$ SST turbulence model, as shown in Eq. (32). The choice of turbulence model has been based on existing, validated numerical research for aero engine ICD intercoolers [33] (including diffuser, crossover, and contraction ducts), short annular diffusers [56], and a review on heat exchanger CFD modeling by Bhutta et al [55]. Additionally, the turbulence model will be further validated in the present paper for its ability to predict the flow in annular diffusers (see Section 3.2). The employed

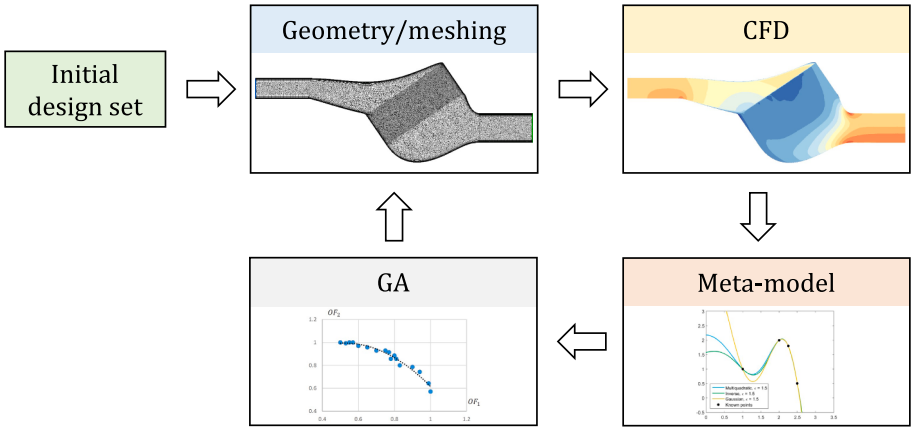

Fig. 6. Layout of the optimization framework.

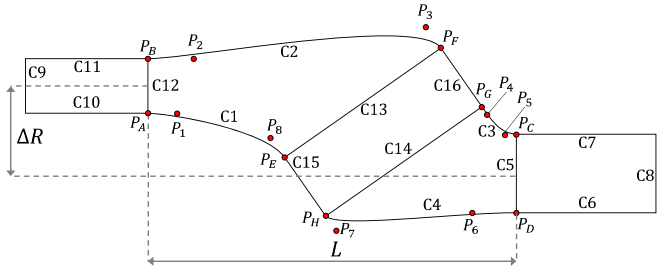

Fig. 7. Bézier curves C# and control points P_i used for defining the duct geometry.

algorithm is Fluent's pressure based solver, using the coupled scheme, and the second order upwind discretization schemes, as is suggested by Fluent's documentation [57]. Gradients are discretized using the Least Squares Cell Based approach.

$$\frac{\partial \boldsymbol{Q}}{\partial t}+\frac{\partial \boldsymbol{F}_j}{\partial x_j}=\boldsymbol{H} \tag{32}$$

$$\boldsymbol{Q}=\begin{bmatrix}\overline{\rho}\\ \overline{\rho}\widetilde{u}_i\\ \overline{\rho}\widetilde{e}_0\\ \overline{\rho}\widetilde{k}\\ \overline{\rho}\widetilde{\omega}\end{bmatrix}\boldsymbol{F}_j=\begin{bmatrix}\overline{\rho}\widetilde{u}_j\\ \overline{\rho}\widetilde{u}_j\widetilde{u}_i+\overline{p}\delta_{ij}-\tau_{ij}+F_i\\ \widetilde{u}_j\left(\overline{\rho}\widetilde{e}_0+p\right)-\lambda_{eff}\dfrac{\partial \widetilde{T}}{\partial x_j}-\widetilde{u}_i\tau_{ij}+S_h\\ \overline{\rho}\widetilde{u}_j\widetilde{k}-\Gamma_k\dfrac{\partial \widetilde{k}}{\partial x_j}\\ \overline{\rho}\widetilde{u}_j\widetilde{\omega}-\Gamma_\omega\dfrac{\partial \widetilde{\omega}}{\partial x_j}\end{bmatrix}\boldsymbol{H}_j$$

$$=\begin{bmatrix}0\\0\\0\\G_k-Y_k\\G_\omega-Y_\omega+D_\omega\end{bmatrix}$$

Additional terms and modeling constants are given in [57]. The working fluid is set to dry air, represented as an ideal gas. The inlet boundary condition (see Fig. 8) is defined using a prescribed total temperature, total pressure, and a turbulence intensity of 5 %. The hub and shroud walls are set as no-slip and adiabatic. The outlet boundary condition was set as a mass flow outlet. The required boundary condition values are chosen from Table 8 for the Top-of-climb (ToC) operating point. The streamwise pressure drop (parallel with L_x in Fig. 3) of the flow due to the presence of the heat exchanger is incorporated into the CFD model through an inertial resistance factor λ, as was previously done by [27–29]. This factor is shown in Eq (33) and is calculated using output data from the heat exchanger conceptual design (Section 2.1.1), with the pressure drop obtained from Eq. (26) and flow conditions at the inlet of the HEX. The air is forced to flow along the direction of the fins of the heat exchanger by means of an inertial resistance factor in the transversal direction (parallel with L_y in Fig. 3), which is set as three orders of magnitude greater than the corresponding streamwise inertial resistance factor.

$$\lambda=\frac{\Delta p_{air}}{\frac{1}{2}\rho_{1,air}v_{1,air}^2L_x}$$

$$v_{1,air}=\frac{\dot{m}_{air}}{A_{inlet}\rho_{1,air}} \tag{33}$$

The streamwise and transversal resistance factors are included in the CFD governing equations (Eq. (32)) though the factor C_i, which can be found in the momentum equation source term $F_i = C_i\rho|\boldsymbol{u}|u_i/2$. The inclination of the HEX is used to project the resistance factors into the corresponding components of C_i. (see Fig. 3). Heat transfer was incorporated into the CFD model by using the energy source term $\dot{q}$ in Eq. (34) that acts as a heat sink in the HEX domain (see Fig. 8) and is incorporated into the governing equations using the term S_h in the energy equation. It is calculated using the heat flow Q(Eq. (9)) from conceptual design and the heat exchanger volume V_{HEX} (Eq. (2)):

$$\dot{q}=Q/V_{HEX}\left[\mathrm{W/m^3}\right] \tag{34}$$

Each conducted CFD simulation was typically run using 4 cores on an Intel Xeon W-2275 CPU, taking approximately 5–10 min to finish depending on size of the mesh and flow instabilities. Simulations were terminated early if the residuals reached below 10^{-8}, otherwise they kept iterating until reaching 1200 iterations, which has been observed to be sufficient for the residuals to level out.

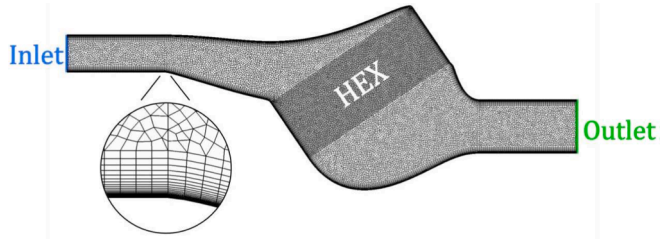

Fig. 8. An example of a computational mesh for an AR 4 heat exchanger simulation. The dark grey region corresponds to the location of the HEX domain.

The CFD results are post-processed, and the values of the objective functions (total pressure loss and HEX inlet flow non-uniformity) are extracted and used to generate a *meta*-model by means of Radial Basis Functions (RBF) [58]. During post-processing, results were kept for cases where the maximum residual was below 10^{-4}, while the remainder were discarded. This allowed for removing the cases with bad convergence while simultaneously keeping enough data to inform and update the meta model. The *meta*-model is then used by the Genetic Algorithm (GA) (based on NSGA-II [59]), which finds new designs that minimize the objective functions. The GA attempts to find optimal designs based on the response for the *meta*-model, using a population size of 100 individuals which is run for 100 generations. For each generation the following processes are carried out in order to advance the population; ranking, tournament selection, crossover, mutation, and elitism, which are described in detail by Montero et al. [53] and Deb et al. [59]. After the GA has run for 100 generations it then outputs 20 new designs, which are then meshed, simulated, and added to the *meta*-model which will be used by the GA once again. This process continues until no improvement is reached for the objective functions.

The numerical approach employed for the duct design and aerodynamic optimization is an important element of the present study, hence it requires further justification with respect to its usage as well as associated limitations. The usage of 2D axisymmetric RANS provides relatively fast and sufficiently accurate results for use in a large aerodynamic optimization effort. Lower fidelity models such as the Euler equations would not capture viscous or turbulent effects, while higher order models or dimensionality (3D) would increase computational cost to prohibitive levels, especially when thousands of CFD simulations are required in the optimization. Three-dimensional effects, such as the inclusion of swirl profiles at the inlet of the diffuser, are known to delay endwall separation and to positively impact on the pressure recovery [60]. This would converge into more aggressive duct designs, which would be prone to separation at low levels of inlet swirl. Therefore, it was decided that the optimization studies were to be performed with zero swirl at the inlet, thereby increasing the stringency of the diffuser design requirements. Still, the inclusion of 3D effects and the employment of higher-fidelity methods, such as LES (Large Eddy Simulation) or DES (Detached Eddy Simulation), is required, together with an associated validation model to accurately predict the fluid flow in design and off-design conditions during more detailed design phases of the heat-exchanger.

2.3. Engine system model and aircraft trade-factors

To investigate the integrated performance of the proposed heat-management concepts, system-level models are developed for a liquid hydrogen propulsion system for entry into service (EIS) in 2050. The system comprises thermodynamic and conceptual design models of a hydrogen-fueled geared turbofan engine, as well as a hydrogen aircraft performance model.

For engine modeling purposes, Chalmers' in-house engine simulation tool GESTPAN (General Stationary and Transient Propulsion Analysis) [61] is used. GESTPAN is a gas turbine simulation system with the capability of predicting design, off-design, and transient performance of existing and novel aero-engine concepts. GESTPAN has been extensively used and validated across several gas turbine aero-engine applications, including intercooling and recuperation [34,36,37,62–65]. Recently the tool was extended to model the performance of hydrogen-fuel feed and heat management systems in [12]. REFPROP [45] is used to model the thermophysical properties of hydrogen from cryogenic conditions in the propellant tanks to the combustor inlet condition. Additionally, it is also used for representing the performance of real compression processes in the fuel system pumps. Combustion and combustion products are modelled using temperature–pressure and fuel–air-ratio-dependent tables generated using NASA CEA [66].

Conceptual design is carried out using Chalmers' in-house tool WEICO (Weight and cost). WEICO allows for estimating the power plant weight and flow-path size, allowing to introduce the impact of component size in the 0D thermodynamic performance. Intercooling is expected to increase the core specific power at a given thrust, hence impacting the turbomachinery size. The incurred size reduction might have a detrimental impact on the performance of the last stages of the high-pressure compressor (HPC). As the blades get smaller, for a constant rotor gap size, the relative impact of the tip-leakage losses on the spanwise loss distribution grows bigger. This can have a severe impact on the overall performance of the entire machine and even deny any benefits that might arise from increasing the compressor pressure ratio. To properly account for such an effect, corrections are applied to the polytropic efficiency using the last stage blade height H_{blade} in Eq. (35) [67]:

$$\eta_{p,\mathrm{HPC}} = \eta_{p,0,\mathrm{HPC}} + \Pi\left(0.0532 - \frac{0.5547}{H_{blade}} - \frac{1.7724}{H_{blade}^2}\right) \tag{35}$$

Here H_{blade} is in mm and Π is a correction factor set to 1 for the HPC and 0.5 for the high-pressure turbine (HPT) as suggested by Rolt et al. [67].

Intercooling impacts NO_x emissions by reducing the HPC outlet temperature for a given engine overall pressure ratio. Here, the Emission Index of NO_x (EINOx) is estimated for a micromix combustor using a correlation for dry air derived in the ENABLEH2 project [68]:

$$EINOx = 0.0864\, p_3^{0.4} e^{T_{31}/191} \phi^{1.95} [\mathrm{g/kg}]\mathrm{fuel} \tag{36}$$

In the equation above p_3 is the HPC delivery pressure in kPa and ϕ is the combustion chamber equivalence ratio. It should be noted that the EINOx correlation Eq. (36) was derived for a constant fuel temperature of 450 K. Hence, Eq. (36) does not include the effect of varying fuel temperature. Therefore, T_{31} is the corrected inlet temperature to include the effect of fuel temperature by assuming adiabatic mixing at constant pressure:

$$T_{31} = T_{H2}\frac{c_{p_{H2}}\dot{m}_{H2}}{c_{p_{air}}\dot{m}_{air} + c_{p_{H2}}\dot{m}_{H2}} + T_{air}\frac{c_{p_{air}}\dot{m}_{air}}{c_{p_{air}}\dot{m}_{air} + c_{p_{H2}}\dot{m}_{H2}} \tag{37}$$

where T_{31} is the fuel–air mixture temperature, in K.

2.3.1. Aircraft trade-factors

Linear trade-factors have been created for the 2050 hydrogen short-medium range (SMR) aircraft to properly account for the integrated effects of the new propulsion units on mission fuel burn. The aircraft concept used in the present study is illustrated in Fig. 9, and it was proposed as a possible solution for medium to long range aircraft configurations where fuel volume requirements converged in designs with above-fuselage-mounted cylindrical tanks. More details about the assumptions, conceptual design and performance can be found in [69].

The mission characteristics and flight profile are included in Tables 3 and 4, respectively. It is noted that to properly model the aircraft design response for the variations in engine performance parameters, engine and nacelle scalability with thrust was included in the present model, in terms of size and weight. Afterwards, important parameters relating to engine specific thrust and specific fuel consumption were independently varied to determine the linear response of the aircraft model in design and off-design conditions. The resulting linear trade-factors are provided with respect to the design point conditions listed in Table 5.

The computed trade-factors reflect the impact of the engine-specific parameters on the whole aircraft fuel burn performance (fuel quantity is scaled to ensure that the mission range/payload is satisfied). For example, looking into Table 6, one can derive that a 1 % reduction in specific fuel burn consumption (SFC) returns a 1.4 % reduction in fuel burn (FB) for the design mission. Reduction in specific fuel consumption reduces other requirements such as hydrogen tank weight, structural weight, and wing size.

The following equations are generally applicable for the SMR aircraft, for parameter ranges given in Table 3, but the nonlinearity

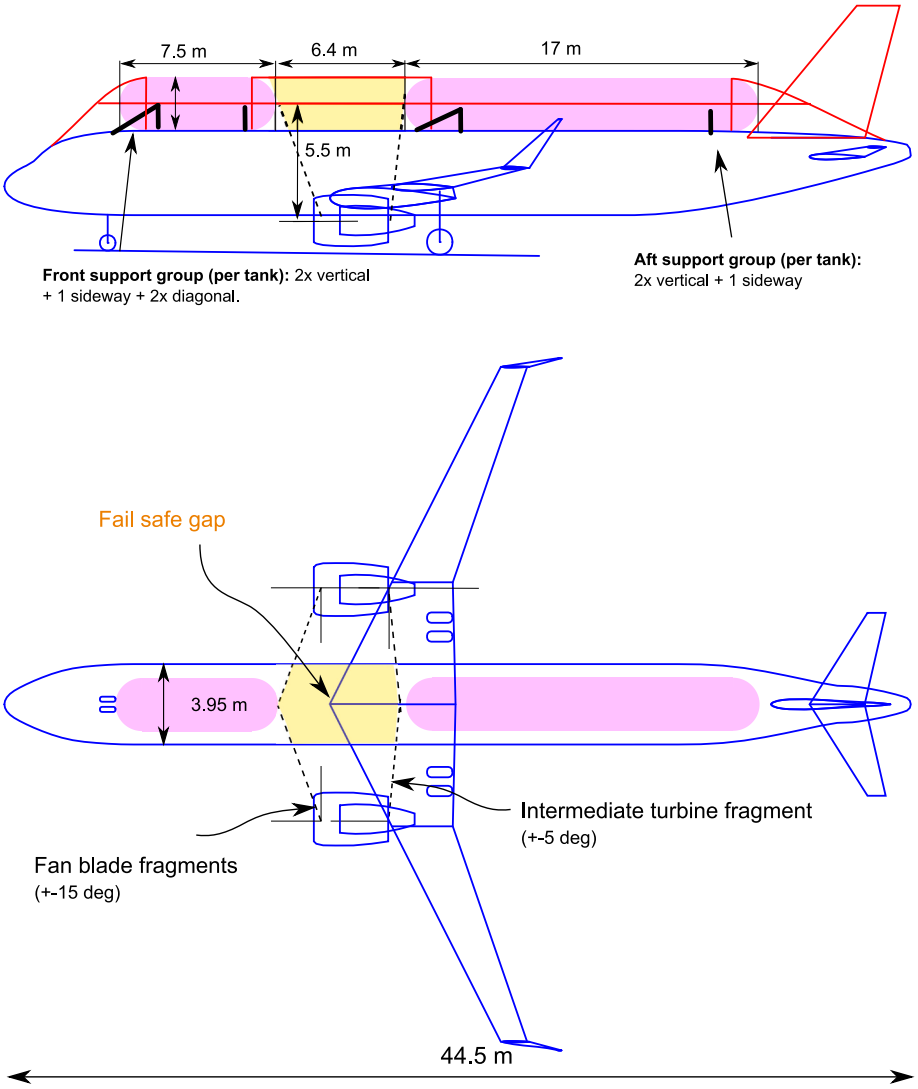

Fig. 9. Short-medium range (SMR) aircraft with PVC insulated tanks mounted above the pressurized fuselage.

Table 3
SMR range aircraft mission characteristics.

Parameter	Value
Design Range [NM]	3000
PAX (design)	200
Payload [kg]	21,000
Cruise Mach	0.75
Climb Mach	0.75
Initial cruise altitude [ft]	35,000

Table 4
Flight Profile.

Parameter	Value
Initial climb up to 10,000 ft	250 CAS
Climb (ISA) after 10,000 ft	300 CAS or M075
Cruise (ISA)	M0.75
Descent (ISA)	300 CAS or M075
Contingency	5 % Trip Fuel
Diversion	100 NM
Diversion altitude	25,000 ft
Hold	30 min
Hold altitude	1500 ft

shown seems to allow for an applicability for a wider range variation. The total fuel burn variation ($\Delta_{FB,total}$) relative to the given design point conditions can be calculated as follows.

$$\Delta_{FB,total} = \left(1+\frac{\Delta_{FB,W}}{100}\right)\left(1-\frac{\Delta_{FB,SFC}}{100}\right)-1 \tag{38}$$

where the relative SFC ($\Delta_{FB,SFC}$) contribution can be estimated using the following correlation:

$$\Delta_{FB,\mathrm{SFC}} = 1.40348\cdot\Delta_{\mathrm{SFC}}^{0.94498} \tag{39}$$

$$\Delta_{SFC} = \left(1-\frac{\mathrm{SFC}}{\mathrm{SFC}_{\mathrm{ref}}}\right)\cdot 100 \tag{40}$$

where SFC is the computed specific fuel consumption, and $\mathrm{SFC}_{\mathrm{ref}}$ is the reference engine data, see Table 5. The engine mass (kg) contribution ($\Delta_{FB,\mathrm{W}}$) is estimated using the following equations:

Table 5
Reference engine design and performance characteristics.

Parameter	Value
$\mathrm{SFC}_{\mathrm{ref}}$(reference, max cruise @M0.75, 35000ft) [mg/Ns]	4.6
W_{ref}, (Reference engine mass) [kg]	3185

Table 6
Trade-factors derived for the year 2050 hydrogen SMR aircraft.

	Design (3000NM)
SFC −1%	−1.4 % FB**
Weight (incl. nacelle)* +500 kg	+2.58 % FB**

*Weight is for a single power plant
**Trip fuel burn, not including taxi

$$\Delta_{FB,W} = 0.00325 \cdot \Delta_W^{1.06550} \tag{41}$$

$$\Delta_W = \left(W - W_{\text{ref}}\right) \tag{42}$$

where W is the computed mass and W_{ref} is the reference engine mass listed in Table 5.

3. Results

This section will first present results for the heat exchanger conceptual design for integration in the intermediate compressor duct (ICD), highlighting design choices and aerothermal performance for two heat exchangers with different diffuser area ratios (AR). It is followed by a validation case of the numerical model using available literature for an annular diffuser design and performance. The subsequent section covers the aerodynamic optimization of the diffusor and contraction ducts, as well as the derivation of pressure loss correlations. The section ends with aero-engine integrated performance calculations and engine conceptual design.

3.1. Heat exchanger conceptual design

Results pertaining to the various steps in the heat exchanger conceptual design are presented in the next subsections. The design will be carried out for two heat exchangers for integration in the ICD with diffuser area ratios four and six (named AR4 and AR6 respectively). For typical operating conditions of aero-engine cores, these area ratios allow for an adequate diffusion of the flow without resulting in prohibitively large heat exchangers and ducts.

3.1.1. Baseline engine

The initial aero-thermal design of the heat-exchanger is carried out using thermodynamic and conceptual design data provided by the baseline engine configuration, as illustrated in the design loop flowchart provided in Fig. 2. The baseline engine is a 30,000 lbf class hydrogen fueled turbofan engine for short-medium range applications, with an EIS year of 2050. The engine performance stems from the assumed technology parameters listed in Table 7, which were derived in project ENABLEH2 and are based on historical trends and the consensus of the industry partners.

The thermodynamic performance is presented in Table 8. The NO_x emission index data, EINOx, are calculated using Eq. (36). It is noted that the baseline engine does not feature a dedicated heat-management system for the fuel, i.e. the fuel is pressurized for injection in the combustion chamber, but not pre-heated and hence the temperature of the fuel entering the combustion chamber is only marginally above its storage temperature. The impact of such a low temperature in the fuel injector design is out of scope in this paper. The boundary conditions required for the aerothermal design of the heat exchanger are also shown in Table 8.

The engine conceptual design drawing and component weight predictions are carried out with WEICO and shown in Fig. 10. The engine includes a 3-stage low-pressure compressor, an 8-stage high-pressure compressor (HPC), a 2-stage high-pressure turbine and a 4-stage low-pressure turbine. The fan tip diameter at the inlet is 2 m, and the last stage blade height of the high-pressure compressor is 12 mm. The provided data in Fig. 10 and Table 8 can now be used to initiate the aerothermal design of the proposed heat-exchanger concepts.

Table 7
2050 performance data assumptions.

Parameter	Value
Fan efficiency (outer fan, isentropic)	94 %
Booster efficiency (polytropic)	92 %
Total cooling air, relative to HPC inlet flow (all points)	10 %
HPC efficiency (polytropic, subject to size correction)	92 %
HPT Efficiency (isentropic)	91 %
LPT efficiency (isentropic)	94 %
T4 [K] (ISA, take-off)	1825

Table 8
Performance data for the baseline hydrogen SMR 2050 engine. For the ICD boundary conditions the subscript 0 refers to stagnation conditions.

	TO	ToC	Cruise
Altitude [ft]	0	35,000	35,000
Mach Number	0	0.75	0.75
Net Thrust [lbf]	30,600	6290	5050
DT_{ISA} [K]	0	0	0
T_3 [K]	871	795	758
T_{31} [K] (after mixing)	760	702	679
p_3 [MPa]	4.10	1.74	1.4
T_4 [K]	1825	1694	1603
BPR	17.1	16.7	18.2
v_{18}/v_8(velocity ratio)	0.72	0.68	0.76
FPR	1.44	1.54	1.45
OPR	40.5	50.2	42.3
Fuel temp (K)	26.66	24.31	24.07
SFC [mg/Ns]	2.35	4.61	4.59
EINOx [g/kg fuel]	22.5	9.8	6.3
Fan diameter [m]		2.0	
Engine weight, including nacelle [kg]		3218	
ICD heat exchanger boundary conditions			
LPC outlet area $[m^2]$	0.0807	0.0807	0.0807
LPC outlet Mach number	0.3831	0.3997	0.3819
Air mass flow [kg/s]	28.86	12.91	11.25
Air p_0 [MPa]	0.2909	0.1189	0.1057
Air T_0 [K]	398.2	356.7	344.1
H_2 mass flow [kg/s]	0.3143	0.1278	0.1022
H_2 p_0 [MPa]	4.200	1.863	1.571
H_2 T_0 [K]	26.66	24.31	24.07

3.1.2. Aerothermal design

The input data needed for the heat exchanger conceptual design include the chosen area ratios, the heat exchanger boundary conditions in Table 8, and the ICD duct corner points (Fig. 10). The chosen design point is ToC since it features the highest Mach number for the diffuser duct inlet (i.e. LPC outlet Mach number). Take-off (TO) and cruise are run as off-design points.

Input design parameters for the heat exchangers are shown in Table 9. The length of the duct is set using the parameter $\Delta R/L$ (see Fig. 7) which relates the length of the duct to the change in mid-radius from inlet to outlet, with higher values being representative of shorter, more aggressive duct designs [70]. The value chosen here is lower than

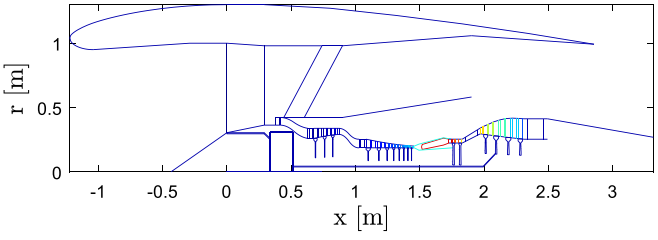

Fig. 10. Schematic engine layout for Y2050 SMR baseline concept.

what is considered conventional ($\Delta R/L = 0.5$) [71,72] but is required for accommodating the volume of the compact heat exchanger. The number of tube banks N_{banks} (see Fig. 4 for description), which determines the length L_x of the HEX, has been set based on prior experience, balancing pressure loss, heat transfer, and volume, and could be optimized at a later stage.

The chosen thermal conductivity k_{fin} for the HEX structural material represents a conservative estimate of what can be found for an aluminum alloy of the 2, 5, and 7-series, depending on material composition. To exemplify, a 5-series alloy such as the 5083 offers good corrosion resistance, relatively high strength, and a thermal conductivity of approximately 120 W/mK [73,74]. The 2219 alloy also offers a thermal conductivity of approximately 120 W/mK [75] and has been previously used in aerospace structures containing cryogenic hydrogen such as the external fuel tank of the NASA Space Shuttle and Space Launch System (SLS) [76,77]. A 7-series alloy such as the 7050 exhibits high strength at high temperatures combined with a high thermal conductivity of 180 W/mK [78]. The final choice of structural material for the heat exchanger matrix will ultimately involve factors such as corrosion resistance, strength, thermal conductivity, and weight, which is outside of the scope of this paper. At this stage it is sufficient to set a representative and conservative value for thermal conductivity in order to perform the heat exchanger conceptual design. The chosen density for the structural material represents the highest value (Alu 2219) among the mentioned aluminum alloys.

The original heat-exchanger geometry, shown in Fig. 4, was isometrically scaled down, thereby decreasing the air-side Reynolds number, and increasing the Nusselt number and heat transfer coefficient. It also increases the available area for heat transfer as the overall HEX volume as defined by $V_{HEX} = L_x L_y L_z$ is kept constant.

Flowing cryogenic hydrogen through the tubes of the HEX at the inlet temperatures specified in Table 8 could result in low enough temperatures on the air side of the HEX to condense or even freeze the oxygen and nitrogen in the air. Therefore, 50 % of the hydrogen at the exit of the HEX is recirculated back and mixed with the incoming colder hydrogen to increase its temperature, thereby avoiding the issues with oxygen and nitrogen freezing and clogging up the air side of the heat exchanger. The recirculation factor of 50 % has been chosen to avoid hydrogen inlet temperatures below 100 K for the HEX. It is noted that in the presence of humid air, 100 K will lead to the condensation and freezing of water in the heat-exchanger walls. If this is to be taken into account, sufficient hydrogen should be re-circulated to achieve an air side wall temperature of at least 273 K.

The resulting heat exchanger conceptual designs are summarized in Table 10. Heat flows in the order of 500 kW were obtained at ToC for both designs. The highest heat flow amounted to almost 1.5 MW for the AR6 heat exchanger at TO, due to the high core air mass flow, pressure, and temperature at this operating point. The lowest amount of heat flow is found at the cruise operating point for both designs due to lower core air mass flows and pressures compared to the other operating points. The core air undergoes a temperature drop ranging from 37.8 to 50.8 K depending on design and operating point, while the hydrogen temperature increase exceeds 260 K for all operating points. Both designs feature air-side total pressure drops at or below 2 %, while the pressure drop for hydrogen is significantly lower (below 0.15 %). These drops in pressure do not account for the losses in the connecting ducts and piping, only losses occurring inside the heat exchanger matrix. Also, the recirculation of hydrogen has led to inlet temperatures $T_{0,inlet,H2}$ reaching above 100 K, as was intended. Relatively high levels of heat exchanger effectiveness are reached for both designs, especially at ToC and cruise, which could be improved further by either isometrically scaling down the heat-exchanger matrix geometry, or by increasing the area ratio of the diffuser. Scaling down would result in smaller tube and fin dimensions, while increasing the area ratio would result in larger ducts, and by extension, a larger engine. The low hydrogen-side pressure drops could allow for a larger tube wall thickness if required in future design iterations. This will decrease the hydraulic diameter $D_{h,H2}$ and lead to an increased convective heat transfer coefficient (and pressure drop) for the tubes, resulting in an increased heat exchanger effectiveness (per Eqs. (21), (23), and (24)).

Table 9
Input parameters for the compact heat exchanger conceptual design.

Parameter	Value
$\Delta R/L$	0.15
N_{banks}	8
N_{passes}	1
$k_{fin}[W/mK]$	120
$\rho_{fin}[kg/m^3]$	2840
ζ	0.5
RC	0.5
Tube wall thickness [mm]	0.254

3.2. Validation

The accuracy of the numerical model to predict the aerodynamic performance of annular diffusers was validated against experimental data taken from [60]. The geometric characteristics of the two tested geometries, A1 and B1, is provided in Table 11. These axisymmetric cases were tested for the non-swirl inlet conditions, for which the inlet velocity profiles can be found in Kumar et al. [60].

Fig. 11 shows the comparison between the computed and experimentally obtained averaged pressure coefficient, $\widehat{C_p} = (\hat{p} - p_{in})/q_{in}$, where $\hat{p}$ is the mass averaged static pressure at a given non-dimensional axial location, x/L, p_{in} is the static pressure at the inlet, and q_{in} is the dynamic pressure at the inlet. In Fig. 11 one can see that the $k-\omega$ SST model results are in good agreement with the experimental data for the A1 geometry. It should be noted that the $\widehat{C_p}$ characteristic in geometry A1 was obtained for an unstalled diffuser, where the flow remains attached to the endwalls. For geometry B1 the diffuser stalls at about 60 % of the shroud. Here the agreement is not as good, falling mostly within the + -15 % CFD uncertainty band. Moreover, the results are not seen to

Table 10
Aerothermal performance for the ICD compact heat exchangers with area ratio 4 and 6. Weight only accounts for the heat exchanger tube and fins. Note that $\Delta T_{0,H2}$ is relative to the hydrogen total temperatures in Table 8. The hydrogen inlet temperature shown here includes recirculation. The pressure variations only account for the loss across the matrix.

	AR4			AR6		
OP	ToC (DP)	TO	Cruise	ToC (DP)	TO	Cruise
$T_{0,inlet,H2}$[K]	111	117	109	118	125	115
$p_{0,inlet,H2}$[MPa]	4.200	1.863	1.571	4.200	1.863	1.571
$T_{0,outlet,H2}$[K]	293	294	285	316	321	305
$p_{0,outlet,H2}$[MPa]	4.196	1.862	1.570	4.194	1.860	1.569
$T_{0,inlet,air}$[K]	398	357	344	398	357	344
$p_{0,inlet,air}$[MPa]	0.2909	0.1189	0.1057	0.2909	0.1189	0.1057
$T_{0,outlet,air}$[K]	356	310	306	353	306	304
$p_{0,outlet,air}$[MPa]	0.2848	0.1171	0.1035	0.2878	0.1180	0.1046
Q [kW]	545	1359	428	588	1484	459
L_x[m]	0.08	0.08	0.08	0.08	0.08	0.08
L_y[m]	0.21	0.21	0.21	0.32	0.32	0.32
L_z[m]	1.53	1.53	1.53	1.53	1.53	1.53
N_{tubes}	1747	1747	1747	1747	1747	1747
$\Delta T_{0,air}$[K]	−41.9	−46.5	−37.8	−45.2	−50.8	−40.5
$\Delta T_{0,H2}$[K]	+266	+270	+261	+289	+297	+281
Δp_{air}	2.08 %	1.52 %	2.04 %	1.07 %	0.74 %	1.05 %
Δp_{H2}	0.09 %	0.08 %	0.08 %	0.14 %	0.14 %	0.13 %
W [kg]	7.4	7.4	7.4	11.1	11.1	11.1
ϵ	80.2 %	72.8 %	81.7 %	87.0 %	80.0 %	87.9 %

improve with subsequent grid refinements. Still, the results show that the implemented model is able to predict the flow in annular diffusers, primarily for attached flow cases, which constitutes the main target of the present study.

The validation results also agree with the findings of earlier studies, experimentally investigating ICD intercoolers [33] (including diffuser, crossover, and contraction ducts), and short annular diffusers [56]. These two independent studies have shown a consistent validation of the $k-\omega$ SST model to predict the performance of axisymmetric annular diffuser designs.

3.3. Duct shape optimization

Two duct shape optimization campaigns were carried out, one for each conceptual design (AR4 and AR6), shown in Table 10, comprising a total of 2400 CFD simulations per campaign. As was described in Section 2.2, the optimization aimed to minimize pressure loss and flow non-uniformity by changing the axial and radial position of the HEX together with the shape of the hub and shroud curves of the diffuser and contraction ducts. The total length of the integrated HEX and ducts was kept fixed.

Pareto fronts for the optimizations are shown in Fig. 12a) and Fig. 13a), from which two cases were chosen for comparison which feature similar flow non-uniformities. These cases are included in sub-figures b) and show the flow diffusing without separating for both designs, followed by an abrupt change in Mach number at the interface between the diffuser and HEX, and then routing the flow through the contraction into the outlet, which flows into the HPC. No large separations are seen in the diffuser, although there seems to be a visible thickening of the boundary layer for the diffusor hub and shroud for the AR6 duct design. Cooling of the core air is relatively uniform as shown in Fig. 14, where the total temperature is shown to decrease along the air flow direction in the HEX. A locally lower total temperature is seen for the AR6 duct at the HEX hub which is probably influenced by the thicker hub boundary layer in the diffusor. This cold region of the flow is transported downstream along the contraction hub, resulting in a more non-uniform temperature distribution (ranging 287–325 K) at the contraction outlet compared to the AR4 design, which had a temperature range of 306–327 K. This constitutes a possible area of improvement in order to obtain a design with more uniform outlet temperatures, which feeds downstream into the HPC and could have an effect on compressor performance by altering the local speed of sound. It is noted that such variations in temperature profile should ideally be accommodated for in the design of downstream compressor stages.

One noticeable difference between the AR4 and AR6 duct designs is the length of the contraction, which is considerable larger for the AR4 design, potentially leading to higher component weight and engine length than necessary. The total pressure loss (as fraction of inlet p_0) for the contractions are relatively similar and correspond to 0.11 % and 0.15 % for the AR4 and AR6 designs, respectively. Therefore, a shorter contraction should be achievable without any significant total pressure loss increase. This redesign has been carried out through an additional optimization campaign where the length and shape of the contraction was allowed to vary while the diffuser duct design was kept fixed. Fig. 15 shows the resulting AR4 geometry which has seen a 35 % reduction in length compared to the original duct design but at a cost of a slightly increased total pressure loss and flow non-uniformity (Table 12).

A comparison of the performance for the short AR4 design compared to the earlier AR4 and AR6 designs is provided in Table 12, showing that the AR6 features the lowest flow non-uniformity and lowest overall total pressure drop ($\Delta p_{0,total}/p_{0,inlet}$). Breaking down this pressure drop into its constituent parts as shown in Table 12 reveals that the diffusor and contraction pressure losses are small, while the majority of the losses stem from the transversal velocity at the inlet of the HEX, i.e. the velocity component perpendicular to HEX inlet face (or parallel with curve C13 in Fig. 7). For these designs the HEX is inclined, and therefore the flow has a certain incidence relative to the fins of the HEX, meaning that the kinetic energy of the transversal velocity of the incoming flow will become a loss. These losses can potentially be decreased by fine-tuning the design of the heat exchanger fins, either by tweaking the leading edge of the fins or by employing curved fins.

Velocity profiles have been extracted on axial planes in the diffusers of the AR4 and AR6 geometries, see Fig. 16. The location has been chosen relatively close to the HEX inlet face of the AR4 geometry, resulting in an AR of 1.4, and will be compared to the equivalent location on the AR6 diffuser. It can be seen that the boundary layer thicknesses at the hub and shrouds are of similar size. One would expect the velocities to be of similar magnitude since they are at the same AR location in the diffuser. This is true close to the hub, but there is a relatively large velocity difference in the vicinity of the shroud, which can be attributed to the convex shape of the AR4 diffuser shroud. The radial velocities are also similar near the hub for both designs but start to differ when approaching the shroud because of the different slopes of the AR4 and AR6 shroud curves at the chosen sampling locations.

The duct geometries obtained here are also applicable for heat exchangers employing other coolants as long as the same heat exchanger matrix is used (9.1–0.737-S). The need for this might arise if the engine designer wishes to employ a secondary fluid such as helium, carbon dioxide, or nitrogen as an intermediate coolant in the engine, transferring heat between the hot core air and cold hydrogen in a closed loop. This would eliminate the risk of direct hydrogen leaks into the hot core air stream but would also increase design complexity and engine weight.

The short AR4 as well as the AR6 duct designs will be used to generate pressure drop correlations for system level studies. Henceforth, AR4 will refer to the short duct design.

3.4. Mesh study

Before generating pressure loss correlations, a mesh study needs to be carried out for the selected designs in Table 12. The mesh grids used for generating results in Section 3.3 for the AR4 and AR6 designs were used as starting point. The study varied the cell counts for both designs, ranging 60–440 k cells for the AR4 design and 130–700 k cells for the AR6 designs, as seen in Fig. 17. Cases featuring 300 k cells and 485 k cells were then chosen for the AR4 and AR6 design, respectively, for generating pressure loss correlations. These cases featured less than 0.1 % variation in overall total pressure loss over the entire duct compared to the most refined mesh grids. For each chosen case the largest variation was found for the contraction total pressure loss, amounting to 4 % for the AR4 case and 3 % for the AR6 case compared to the most refined meshes. The coarsest meshes for each design shown in this image, which correspond to the cases used in the optimization, show proportional differences in the order of 1 % compared to the finest meshes and strike a balance between accuracy and computational cost for the duct shape optimization.

In Section 2.2 it was mentioned that the first wall node height was set small enough to result in an average y^+ well below 1 on the hub and shroud curves of the ducts. The y^+ distribution along these curves has

Table 11
Geometrical definitions of the annular diffuser geometries used for validation [60]. β denotes the diffuser wall angle for the hub and casing.

Geom.:	$\beta_{hub}[^\circ]$	$\beta_{shroud}[^\circ]$	$R_{hub,inlet}[m]$	$R_{shroud,inlet}[m]$	$R_{hub,exit}[m]$	$R_{shroud,exit}[m]$	AR	$L[m]$	$L/\Delta R$
A1	10	10	0.038	0.0775	0.125	0.164	2.5	0.498	12.6
B1	7.5	10	0.038	0.0775	0.103	0.164	3.6	0.498	12.6

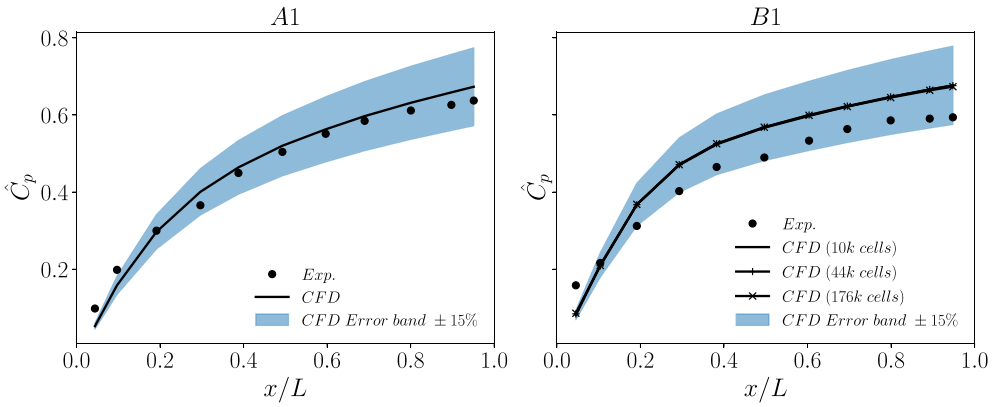

Fig. 11. Comparison between the computed and experimentally obtained averaged pressure coefficient, $\widehat{C_p} = (\hat{p} - p_{in})/q_{in}$ distributions for geometry A1 and geometry B1.

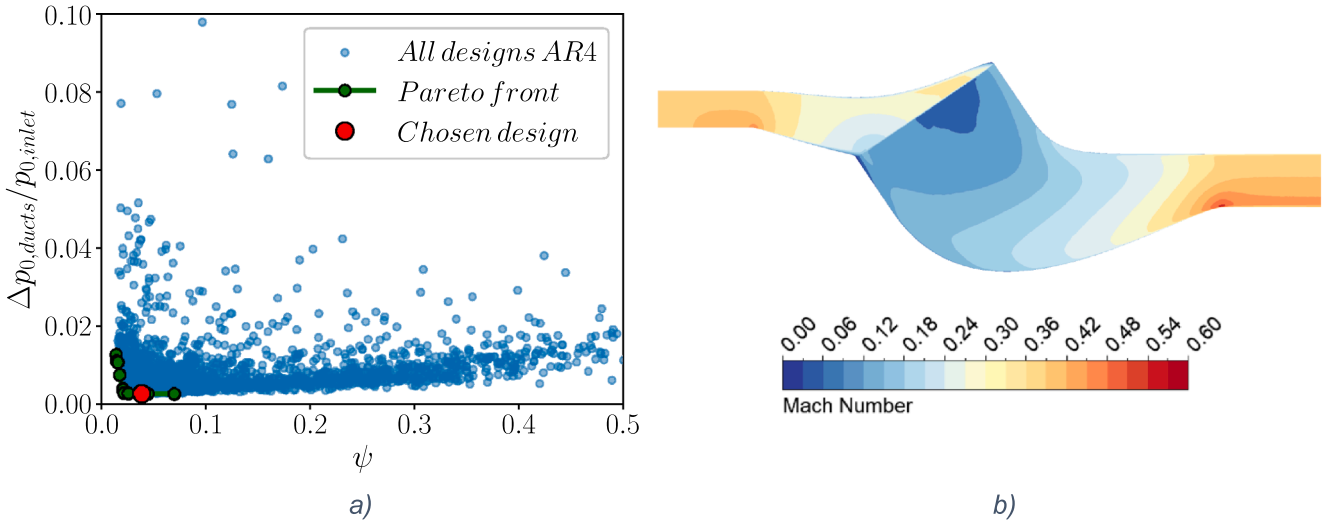

Fig. 12. (a) Pareto front for the ar4 optimization for the two objective functions, flow non-uniformity ψ and duct total pressure loss. (b) Chosen duct design (Case 1792) from the AR4 optimization and its Mach number distribution.

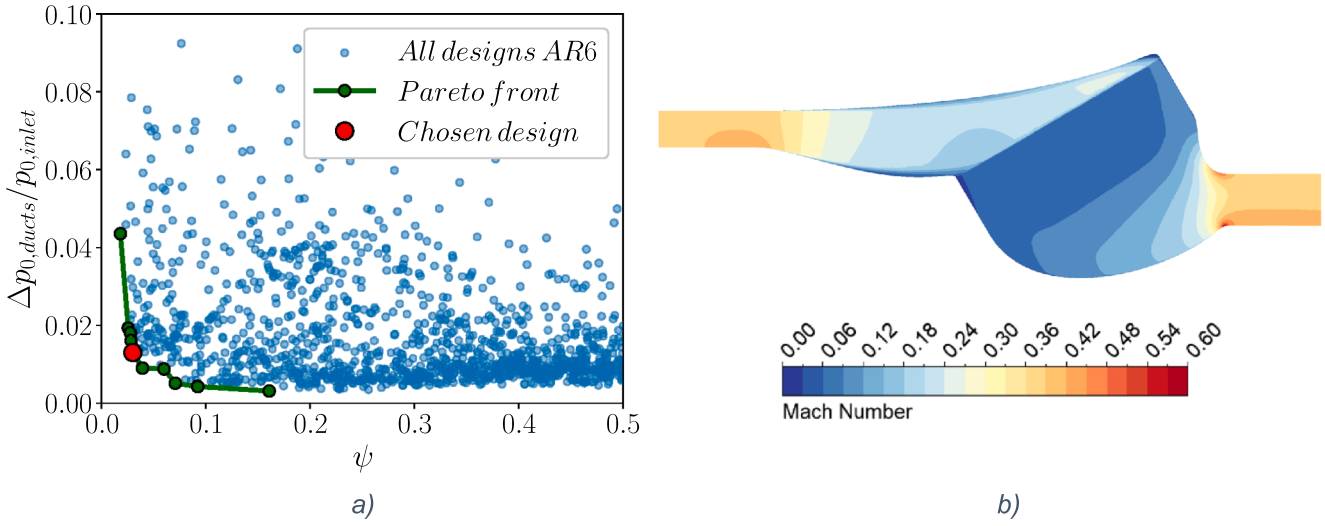

Fig. 13. (a) pareto front for the ar6 optimization for the two objective functions, flow non-uniformity ψ and duct total pressure loss. (b) Chosen duct design (Case 1631) from the AR6 optimization and its Mach number distribution.

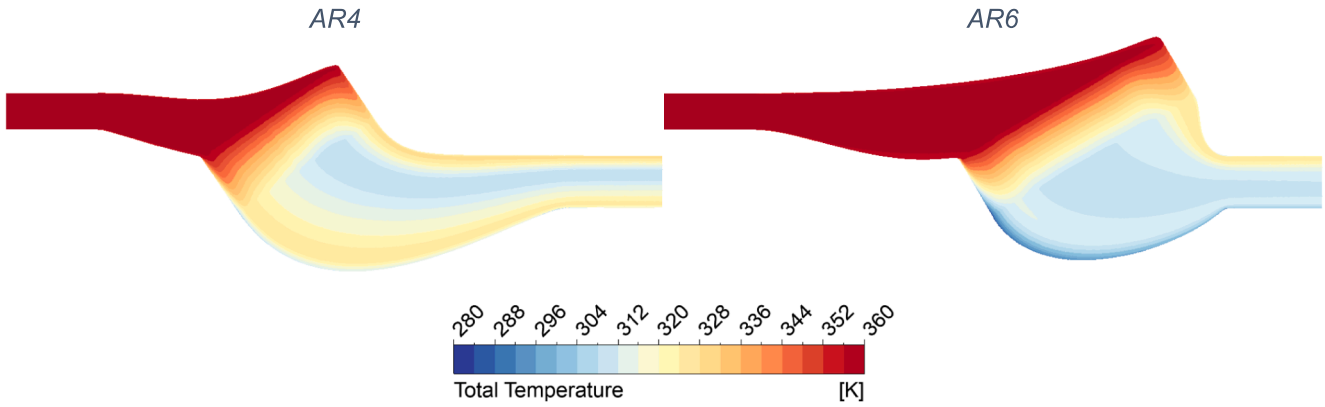

Fig. 14. Total temperature contour for the AR4 and AR6 duct designs.

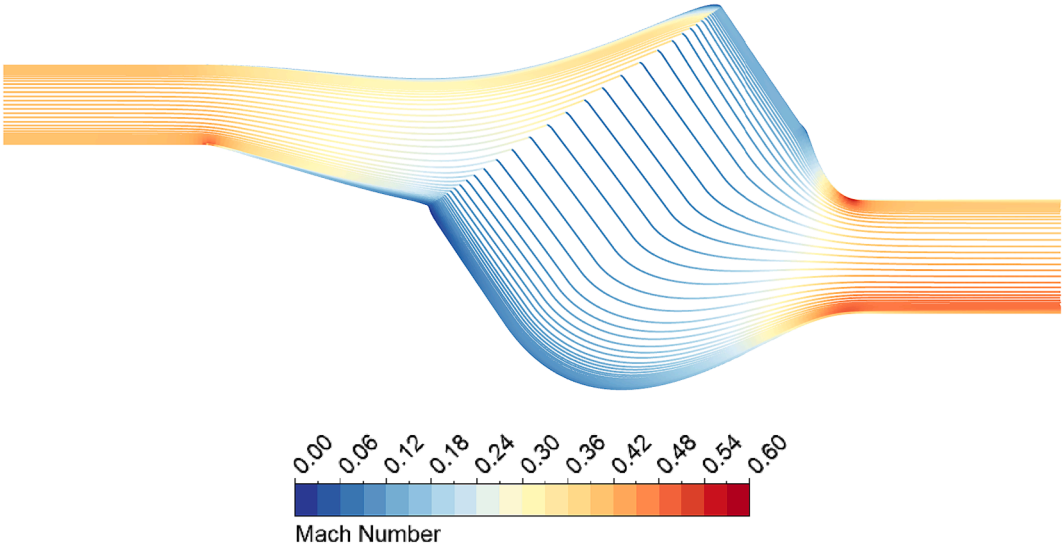

Fig. 15. Streamlines colored by Mach number of the shortened and optimized AR4 duct design.

Table 12
Flow non-uniformity and total pressure breakdown for the three analyzed designs.

	AR4 (short)	AR4 (original)	AR6
ψ	4.74 %	3.86 %	3.02 %
$\Delta p_{0,total}/p_{0,inlet}$	7.92 %	7.23 %	4.29 %
$\Delta p_{0,diffusor}/p_{0,inlet}$	0.22 %	0.20 %	0.33 %
$0.5\rho V^2_{trans}/p_{0,inlet}$	5.01 %	4.43 %	2.65 %
$\Delta p_{0,HEX}/p_{0,inlet}$	2.58 %	2.45 %	1.16 %
$\Delta p_{0,contraction}/p_{0,inlet}$	0.11 %	0.14 %	0.15 %
Duct axial length [m]:	0.375	0.580	0.580

therefore been extracted and plotted in Fig. 18 for the short AR4 design and shows that y^+ is below 0.3 on all walls. The axial distance has been normalized, starting at 0 at the diffuser and ending at 1 at the contraction outlet.

3.5. Pressure loss correlations

This section of the paper revolves around generating pressure drop correlations for the AR4 and AR6 ducts presented earlier. These will be used later in system level performance calculations to assess the impact on engine performance. The correlations were generated by adapting the CFD simulations from the mesh study to allow for varying the dynamic viscosity, and consequently the Reynolds number in the ducts.

The pressure losses in the diffuser and contraction duct have been calculated for a series of duct Reynolds numbers Re_{D_h} to generate pressure loss correlations. For the diffuser, a total pressure loss coefficient $K_{diffuser}$ was defined that consists of two terms; K_{diff} which represents the pressure loss in the diffuser itself and K_{trans} which is the pressure loss due to the transversal velocity component present at the heat exchanger inlet. Both are related to the dynamic pressure at the diffuser inlet:

$$K_{diffuser} = \frac{p_{01} - p_{02}}{p_{01} - p_1} = K_{diff} + K_{trans} = \frac{p_{01} - p_{01b}}{p_{01} - p_1} + \frac{\rho_{1b} V^2_{1b,trans}}{2(p_{01} - p_1)} \tag{43}$$

As seen in Fig. 19, station 1 refers to the diffuser inlet, station 1b to a position just upstream of the diffuser outlet, and station 2 at the diffuser outlet, which assumes that all the kinetic energy of the transversal velocity has become a loss. For the contraction a factor was used which relates the total pressure loss to the dynamic pressure:

$$K_{contr} = \frac{p_{03} - p_{04}}{p_{03} - p_3} \tag{44}$$

where stations 3 and 4 denote the inlet and outlet of the contraction duct. The obtained correlations for the AR4 design are presented in Eqs. (45)-(47). Plots of the of the underlying data and the correlations are shown in Fig. 20.

$$K_{diff} = 0.1584 Re^{-0.1527}_{D_{h,diff}} + \frac{334.0}{Re_{D_{h,diff}}} \tag{45}$$

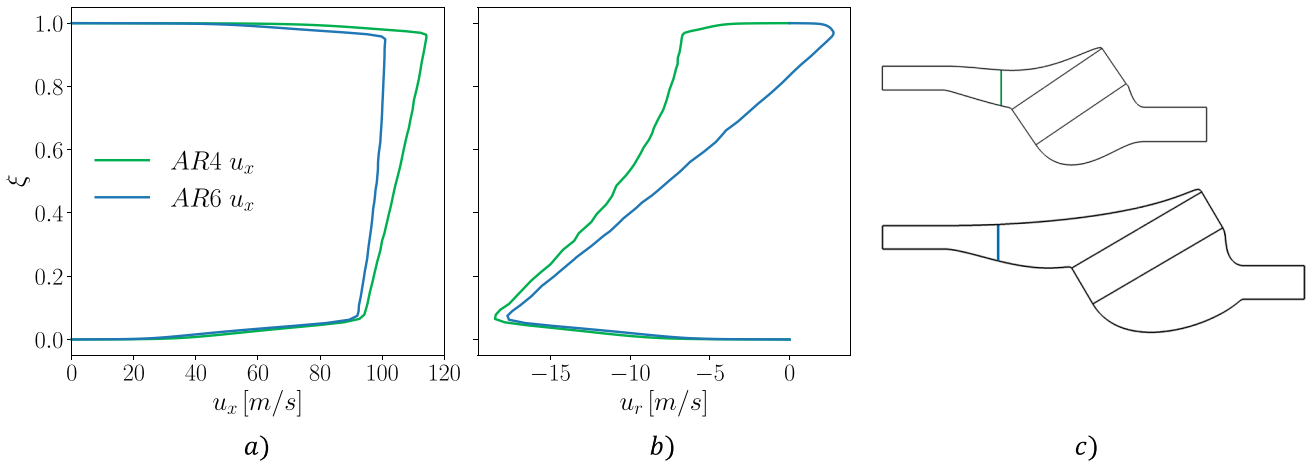

Fig. 16. (a) Axial and (b) radial velocity profiles for the ar4 and ar6 designs on an axial plane, whose cross-sectional area corresponds to an area ratio of 1.4 with respect to the inlet. the locations of the axial planes are shown in (c). the vertical distance ξ has been normalized.

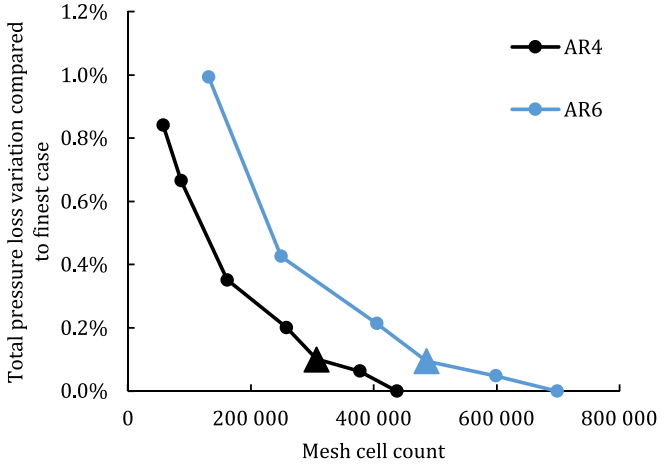

Fig. 17. Total pressure drop variation for the AR4 and AR6 duct designs relative to the finest mesh for each case. Chosen mesh cases for generating correlations are highlighted with a triangle marker.

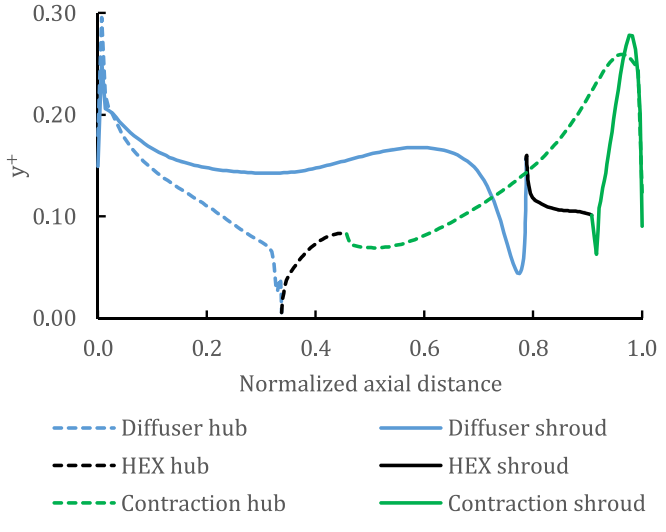

Fig. 18. Distribution of y^+ along the hub and shroud of the diffuser, HEX, and contraction for the short AR4 design.

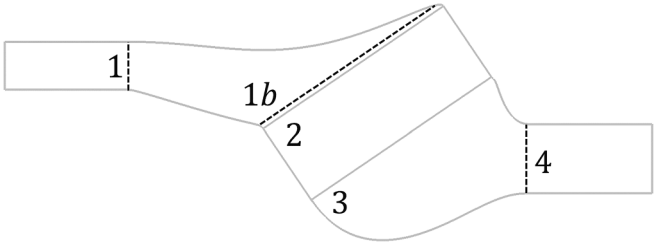

Fig. 19. Station numbering used for the pressure loss correlations.

$$K_{trans} = 0.5183 Re_{D_{h,diff}}^{-0.005126} + \frac{600.1}{Re_{D_{h,diff}}} \tag{46}$$

$$K_{contr} = 0.3633 Re_{D_{h,contr}}^{-0.07585} + \frac{15713}{Re_{D_{h,contr}}} \tag{47}$$

Eqs. (45)–(47) have maximum errors of 0.14 %, 0.04 %, and 4.02 % respectively. The Reynolds number used in (41) and (42) is based on the diameter of the diffuser duct inlet. For the contraction pressure loss the Reynolds number is instead based on the diameter of the contraction duct outlet. The range of validity for the diffuser correlations is $10^5 < Re_{D_{h,diff}} < 4 \times 10^6$ while for the contraction it is $1.4 \times 10^5 < Re_{D_{h,contr}} < 5.7 \times 10^6$.

The obtained correlations for the AR6 design are shown in Eqs. (48)–(50). Plots of the of the underlying data and the correlations are presented in Fig. 21.

$$K_{diff} = 0.2217 Re_{D_{h,diff}}^{-0.1734} + \frac{668.3}{Re_{D_{h,diff}}} \tag{48}$$

$$K_{trans} = 0.2913 Re_{D_{h,diff}}^{-0.007836} + \frac{557.5}{Re_{D_{h,diff}}} \tag{49}$$

$$K_{contr} = 0.5796 Re_{D_{h,contr}}^{-0.05714} + \frac{54354}{Re_{D_{h,contr}}} \tag{50}$$

Eqs. (48)–(50) have a maximum error of 0.79 %, 0.03 %, and 2.44 %. The range of validity for the diffuser correlations is $10^5 < Re_{D_{h,diff}} < 4 \times 10^6$ while for the contraction it is $1.4 \times 10^5 < Re_{D_{h,contr}} < 5.7 \times 10^6$.

The decrease in pressure loss factor for increasing Reynolds number in the diffuser and contraction is typical for internal flows dominated by boundary layer losses, and the trends are similar to what can be found in a Moody chart for pipe flow with smooth surfaces [79]. The smoothness

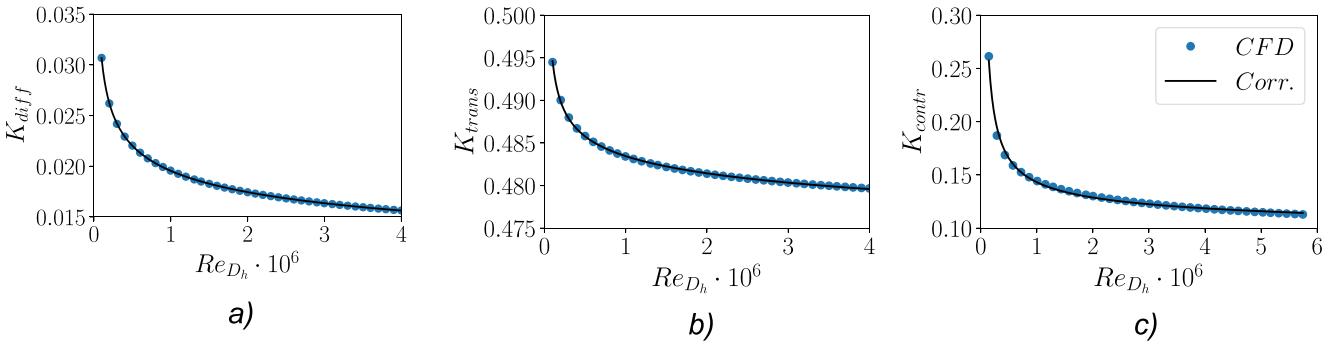

Fig. 20. (a) diffuser total pressure loss factor K_{diff}, (b) transversal velocity loss K_{trans}, and (c) contraction total pressure loss factor K_{contr} for the AR4 duct design. Each point is a CFD simulation while the solid line is the generated correlation.

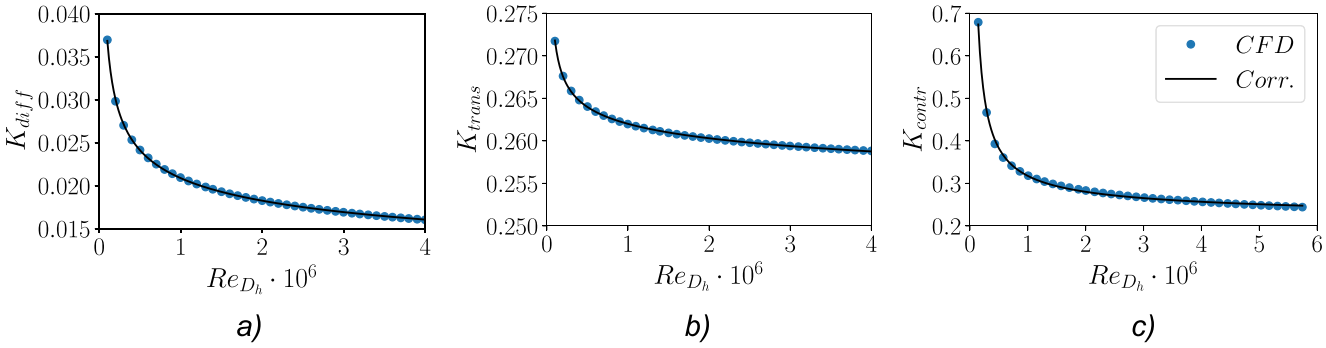

Fig. 21. (a) diffuser total pressure loss factor K_{diff}, (b) transversal velocity loss K_{trans}, and (c) contraction total pressure loss factor K_{contr} for the AR6 duct design. Each point is a CFD simulation while the solid line is the generated correlation.

of the curves also suggests that the flow remains attached without any boundary layer separation, which would otherwise yield a sudden increase in total pressure loss when passing a specific Reynolds number. The seemingly large contraction pressure loss coefficients for either design does not mean that there are large losses occurring in the contraction, instead it is due to the low dynamic pressure at the inlet of the contraction. The largest pressure loss coefficient is as expected due to the transversal velocity at the inlet of the HEX, which is up 30 times larger than the diffuser pressure loss at high Reynolds numbers for the AR4 design. For the AR6 design it is up to 16 times larger. This loss does not feature such a large proportional decrease with increasing Reynolds number, indicating that this loss is more inertial in nature and proportional to the kinetic energy of the flow at the HEX inlet.

It should be noted that the pressure drop correlations presented here could be employed for other heat exchangers and working fluids, such as exhaust gases for a recuperator, as long as the heat exchanger duct and matrix geometry is retained and is correctly scaled.

3.6. Source term approach versus discretized fins

A verification of the source-term based approach used for incorporating heat exchanger pressure losses and heat transfer into the optimization cases has been carried out by comparing the results for the AR4 design with a CFD case with discrete, meshed fins, as shown in Fig. 22. This case includes all 151 fins, all of which are included in the computational mesh. The mesh uses the same cell sizes on the hub and shroud curves as was used for the pressure loss correlation cases in section 3.5 but introduces local refinements near the leading and trailing edges of the fins in order to account for their curvature, as seen in Fig. 22. For the rounded fin leading and trailing edges 10 nodes were used for discretization, while the boundary layer mesh on all walls featured a first node height of 10^{-6} m, yielding an average y^+ of 0.2. The boundary layer mesh featured a growth rate of 1.2 and a maximum of 45 layers. The tubes of the heat exchanger geometry have been omitted from the model to keep the case 2D and the computational mesh at a manageable size of 5.1 million cells. The dominating contributor to the heat exchanger pressure loss, the transversal velocity at the HEX inlet, is still accounted for using this approach. The effect of heat transfer on the flow is accounted for by prescribing the heat flow Q from Table 10 on the walls of the fins.

A comparison of the Mach number and total temperature distributions for the source term and discrete fin cases is shown in Fig. 23. Here it can be seen that the flow velocities for the two types of cases are in good agreement except for a region near the diffusor and HEX hub, which show larger regions low momentum flow, which for the finned case propagate downstream along the contraction duct hub surface. This also leads to locally low temperatures at the hub of the HEX and

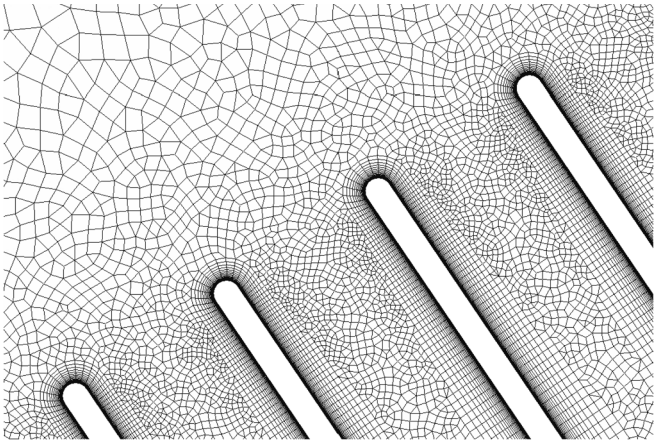

Fig. 22. Close-up of the mesh generated near the leading edge of the fins.

contraction, which is not seen as clearly for source term case. The lowest temperature for the discrete fin case reached 228 K, located on the fin wall closest to the HEX hub and is due to the low momentum flow in this region. The flow temperatures are also approximately 5 K lower for the discrete case at the 75 % radial position of the contraction inlet.

The case with discrete fins experiences a total pressure loss of 7.18 % compared with the 7.93 % for the source term case, which could be attributed to the exclusion of the tubes of the heat exchanger. Nevertheless, the flow properties compare well between the two cases, as can be seen in Fig. 24.

The velocity profiles for the HPC inlet show good agreement between the source term and discrete fin approach. For the contraction inlet profile there is a difference due to the wakes of the heat exchanger fins which create a wide "band" for the plotted curve of the discrete fin approach. Similar conclusions can be drawn for the total pressure profiles, namely that the profile shapes are very similar between the two approaches, albeit separated by an offset since the tubes of the heat exchanger have been omitted in the discrete fin approach, leading to a slightly higher total pressure loss for the source term approach.

As mentioned earlier, the flow enters the heat exchanger inlet at a certain incidence angle relative to the fins. This is shown in Fig. 25 at a location near its hub where the low momentum region mentioned earlier is visible. The incidence angle is the main responsible for the transversal losses that are represented in Fig. 25, where flow separation is visible at the leading edge of each fin, which also applies for the remaining fins further away from the hub. Clearly a better alignment of the fins with the incoming flow is possible and should result in a partial recovery of the transversal kinetic energy, which should be considered in future designs. To conclude, this comparison has shown that the employed source term approach offers a computationally cheap and sufficiently accurate approach to account for the effect of the heat exchanger on the flow, but that detailed flow analysis, particularly at the leading edge of the fins, is required to improve future designs.

3.7. Engine system level performance

The proposed heat exchanger concepts are now evaluated regarding their impact on the whole engine's performance. Specifically, the heat exchangers are incorporated into engine designs based on the models and characteristics described in Sections 2.3 And 3.1.1, i.e. hydrogen fueled, geared turbofans for SMR aircraft with an EIS of 2050. The heat exchanger designs (AR4 and AR6) will be applied on an intercooled engine, and subsequently extended for use in an intercooled-recuperated engine to maximize the cooling potential of hydrogen, thereby evaluating the impact on cycle performance and fuel burn.

The following changes have been done to the heat exchanger designs compared to Table 9 to improve performance:

- The tube wall thickness has been doubled to increase the hydrogen-side convective heat transfer coefficient and pressure drop. Since the designs presented in Table 10 featured very low hydrogen-side pressure drops it allows for an adjustment of this design parameter to allow for higher heat exchanger effectiveness. This is done for both the intercooler and recuperator.
- The structural material of the recuperator has been changed to Haynes 230 due to expected higher gas temperatures in the core exhaust. This material is commonly used in high temperature gas turbine components and is resistant to hydrogen embrittlement. A thermal conductivity of 18.4 W/m K and a density of 8970 kg/m^3 is assumed for this material [80].

It should be noted that neither of these changes impact the previously obtained air-side pressure drop correlations from earlier sections.

3.7.1. Intercooled engines

The computed performance for two different intercooled engine designs, using heat exchangers reported in Section 3.3, are listed in Table 13. The baseline cycle performance, reported in Table 8, is mostly retained but the LPC pressure ratio has been increased in order to

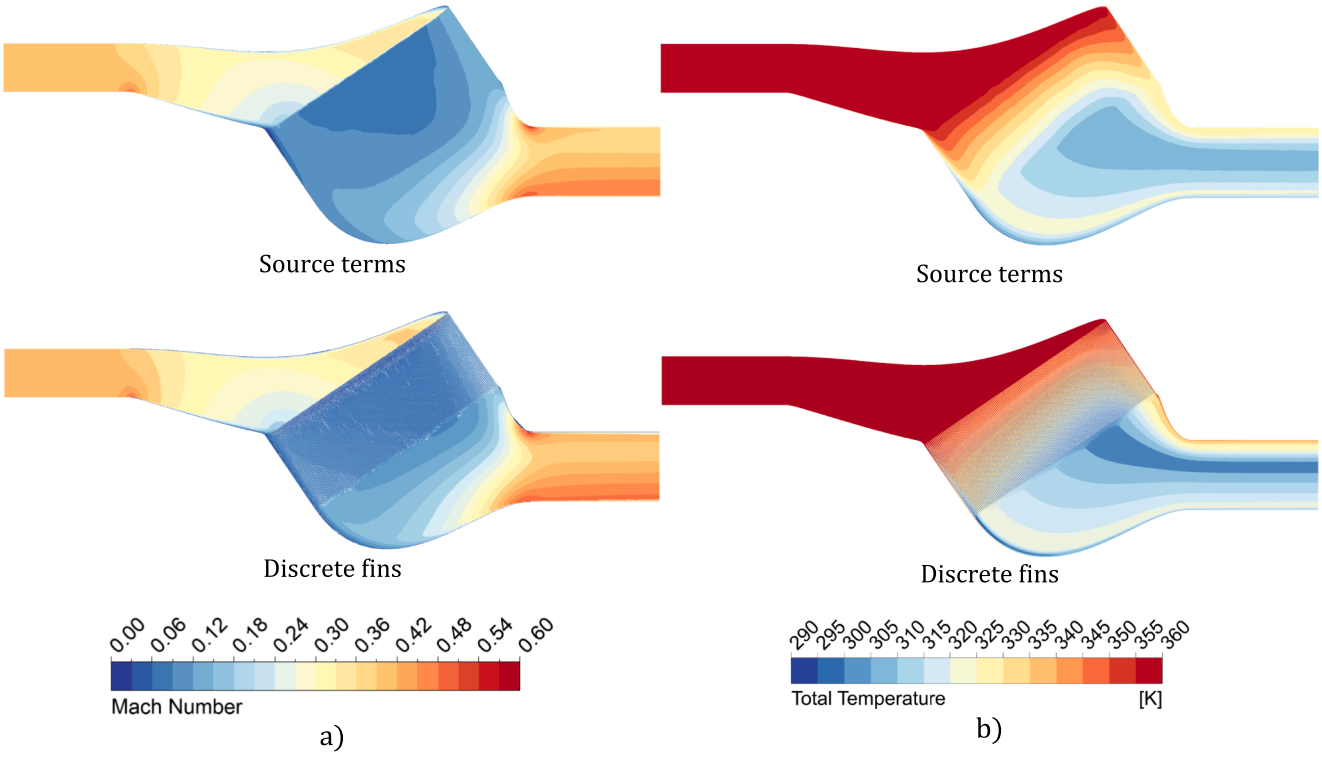

Fig. 23. Comparison of (a) the Mach number and (b) total temperature distributions for the cases employing source terms and discrete fins. It should be noted that the total temperature for the discrete fins case reached lower values than what is shown in the legend, approaching 228 K.

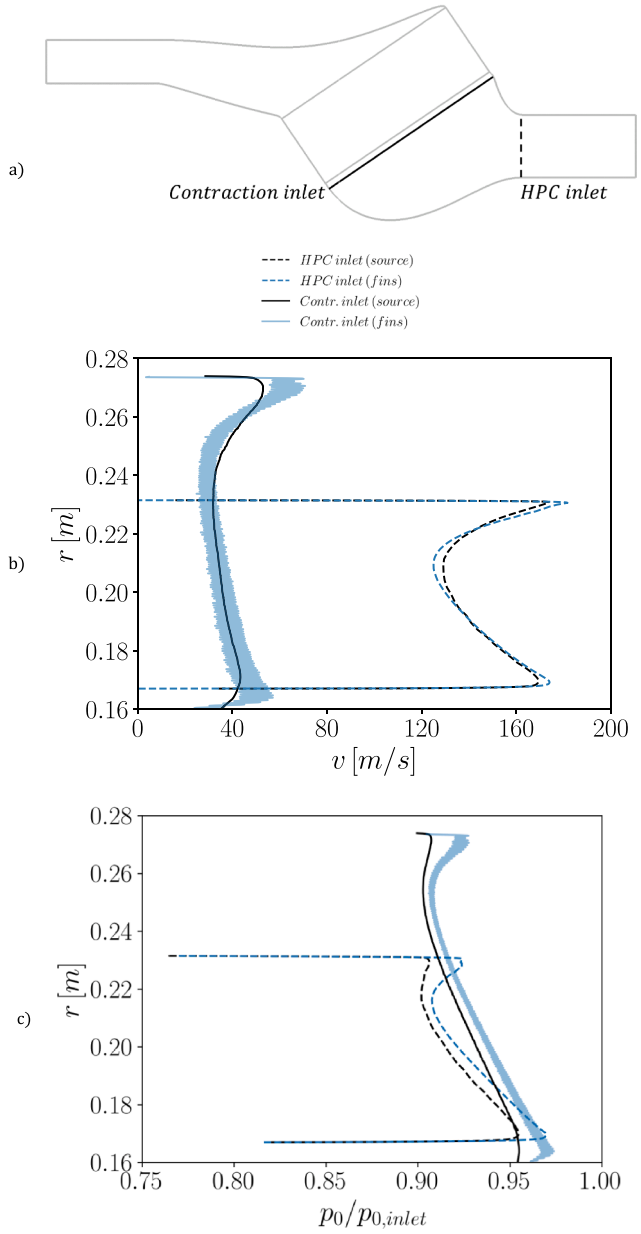

Fig. 24. (a) Location of contraction and hpc inlets in the domain, (b) velocity, and (c) total pressure distributions along the contraction and hpc inlets.

compensate for the added heat exchanger and ducts. The low-pressure system has been rematched to the new core by increasing the bypass ratio (BPR) and keeping the fan pressure ratio constant until the same velocity ratio (v_{18}/v_8) (v_{18}– cold exhaust velocity, v_8 – hot exhaust velocity) was achieved.

Compared to the baseline cycle there are few obvious differences; a decrease in the high-pressure compressor (HPC) outlet temperature (T_{31}) due to the reduction of core air temperature in the intercooler, an increase in bypass ratio (BPR) due to an increase in core specific power, and an increase in fuel temperature due to the pre-heating of the fuel in the intercooler. Consequently, a decrease in SFC compared to the baseline engine is achieved through an increase in fuel enthalpy due to pre-heating, even though it is penalized by the pressure losses associated with the inclusion of new ducts and heat exchangers. Hence, the improvements vary between the two heat exchanger designs due to the different duct performances. The AR4 design resulted in an SFC reduction of about 1.8 %, and the AR6 of about 2.7 %, both in cruise and relative to an uncooled engine.

It should be noted that this analysis does not allow to fully explore the impact of intercooling on cycle performance. Intercooling leads to reduced temperatures at similar OPR levels, permitting increases in pressure ratio until temperature limitations or scale effects on component efficiencies deny further improvements. The lower HPC outlet temperatures could also allow for a reduced turbine cooling air requirement. Neither of these possibilities are addressed in the present study. Nevertheless, the provided data sets a baseline level for further intercooling studies, where the full impact on cycle performance can be quantified. Regarding NO_x emissions, it is observed that intercooling allows to reduce EINOx substantially, especially during TO, as exemplified by the 34 % reduction reached for the AR6 intercooler. It should be further noted that the results presented here are compared with an engine without any fuel pre-heating. For practical reasons one would expect that a fuel pre-heater is required for the baseline engine, such a system could rely on burning a small portion of compressed air and fuel to pre-heat the fuel prior to the main combustor [81].

3.7.2. Intercooled-recuperated engines

The performance data calculated for intercooled-recuperated engines can be found in Table 14. Unlike the intercooler, the recuperator utilizes only half of the core airflow and discharges the cooler exhaust gases through a separate nozzle. Consequently, thrust is generated by the cold nozzle, hot nozzle, and the recuperator exhaust nozzle. This could potentially introduce an additional parameter for optimization, namely the proportion of core air used to pre-heat the fuel at the exhaust. However, this aspect was not explored in the current study. The pressure ratio in the LPC is again raised to compensate for the pressure drop across the intercooler in order to maintain a constant OPR. Similarly, the low-pressure system is adjusted to match the new core by increasing the BPR, while keeping the fan pressure ratio constant until the baseline velocity ratio is attained.

A comparison between the intercooled-recuperated concept to the baseline engine highlights important differences in the cycle data. These differences include a decrease in the HPC outlet temperature due to reduced core air temperature by the intercooler, an increase in BPR due to higher core-specific power, and elevated fuel temperature due to pre-heating within the intercooler and the recuperator. Relative to the intercooled engines, the intercooled-recuperated cycles result in increased reductions in SFC that are mainly driven by the increased fuel temperatures. For example, a reduction of SFC in the order of 5.3 % was achieved for the intercooled-recuperated AR6 cycle at cruise, whereas the intercooled engine provided only 2.7 %. Similar to the intercooled engine studies mentioned earlier, this analysis does not fully explore the extent of heat management potential within the hydrogen fuel system. Nonetheless, it serves as a baseline for future cycle optimization studies using the newly available design parameters. Regarding NOx emissions, it is observed that intercooling combined with recuperation leads to a reduction in EINOx ranging from approximately 23 % to 37 % depending on the operating point and concept. This reduction is driven by decreases in combustor inlet temperature and in the fuel–air ratio, which lowers the combustion equivalence ratio.

Table 15 lists the operating pressures and temperatures in the recuperator for the investigated design and off-design points. Overall, the temperatures are higher across the heat exchanger compared to the ICD heat exchanger, which motivates the change of material from an aluminum alloy to Haynes 230. This material is typically employed in high-temperature components in gas turbines due to its resistance against corrosion and hydrogen embrittlement, making it a suitable candidate for the recuperator heat-exchanger.

The heat transfer performance is based on the heat-exchanger correlations provided by Kays and London [41] with an error band of 10 %, derived for the heat-transfer coefficient from a Taylor expansion of Eq. (11). When the ±10% uncertainty band is introduced in the system level model, it results in about ±0.02% to ±0.03 variation in SFC for the

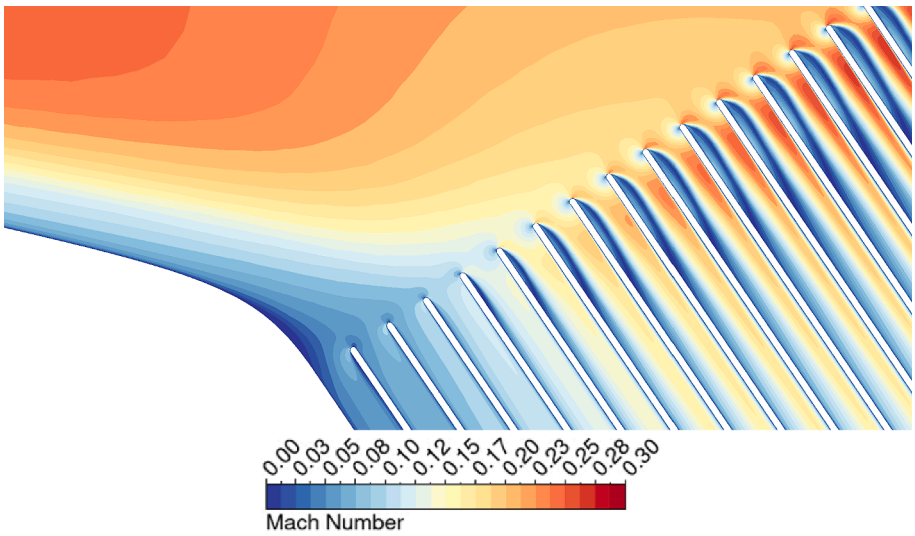

Fig. 25. Mach number contour near the heat exchanger hub and fin leading edges.

Table 13
Performance data for the intercooled hydrogen engine concepts. The intercooler pressure loss includes the losses from the diffuser, contraction, and heat exchanger matrix.

	Intercooled AR4			Intercooled AR6		
	TO	ToC	Cruise	TO	ToC	Cruise
Altitude [ft]	0	35,000	35,000	0	35,000	35,000
Mach Number	0	0.75	0.75	0	0.75	0.75
Net Thrust [lbf]*	30,600	6290	5050	30,600	6290	5050
DT_{ISA} [K]	0	0	0	0	0	0
Intercooler effectiveness	83 %	90 %	86 %	89 %	94 %	92 %
Intercooler Q [kW]	1566	613	459	1625	626	474
Intercooler pressure loss	8.5 %	8.8 %	7.8 %	3.8 %	4.4 %	3.9 %
T_{31} (after mixing) [K]	679	629	613	664	617	601
p_3 [MPa]	4.09	1.74	1.46	4.1	1.75	1.47
T_4 [K]	1825	1700	1620	1825	1702	1622
BPR	18.3	17.9	19.6	18.8	18.3	20.2
FPR*	1.44	1.54	1.45	1.44	1.54	1.45
OPR*	40.5	50.2	42.3	40.5	50.2	42.3
T_{fuel} [K]	344	332	310	362	343	324
SFC [mg/Ns]	2.29	4.52	4.51	2.26	4.47	4.47
Δ SFC (relative to baseline)	−2.7 %	−2.0 %	−1.8 %	−3.9 %	−3.0 %	−2.7 %
EINOx [g/kg-fuel]	15.69	7.25	5.34	14.86	6.97	5.16
Δ EINOx (relative to baseline)	−30 %	−26 %	−21 %	−34 %	−29 %	−24 %

[1]Data kept constant

intercooled and intercooled-recuperated designs, respectively. Regarding the uncertainty related to the aerodynamic performance of the ducts, experimental data is not available for the present design. Still, from the validation results in Section 3.1 and matrix friction loss data available in Kays and London [41], a conservative uncertainty band of ± 10% can be assumed for the pressure losses. This results in ±0.2% in SFC for the intercooled AR4 design and ±0.12% SFC variation for the intercooled AR6 design. Regarding the intercooled-recuperated architectures, the ±10% variation in pressure loss in the heat-exchanger contributes to about ±0.72% variation in SFC for the AR4 design and to ±0.37% variation in SFC for the AR6 design.

Table 14
Performance data for the intercooled-recuperated hydrogen engine concepts. The intercooler and recuperator pressure losses include the losses from each diffuser, contraction, and heat exchanger matrix.

	Intercooled-Recuperated AR4			Intercooled-Recuperated AR6		
	TO	ToC	Cruise	TO	ToC	Cruise
Altitude [ft]	0	35,000	35,000	0	35,000	35,000
Mach Number	0	0.75	0.75	0	0.75	0.75
Net Thrust [lbf]*	30,600	6290	5050	30,600	6290	5050
DT_{ISA} [K]	0	0	0	0	0	0
Intercooler effectiveness	85 %	91 %	86 %	90 %	95 %	93 %
Recuperator effectiveness	77 %	91 %	94 %	84 %	95 %	97 %
Intercooler Q [kW]	1534	609	451	1579	611	465
Recuperator Q [kW]	1675	663	535	1741	664	519
Intercooler pressure loss	7.7 %	8.7 %	7.9 %	3.7 %	4.3 %	3.9 %
Recuperator pressure loss	8.8 %	17.8 %	16.0 %	4.5 %	9.0 %	8.4 %
Recuperator BPR	1	0.97	1	1	0.98	1.01
T_{31} (after mixing) [K]	691	643	625	677	629	611
p_3 [MPa]	4.09	1.76	1.48	4.09	1.75	1.47
T_4 [K]	1825	1706	1626	1825	1706	1625
BPR	18.1	17.6	19.3	18.6	18.0	19.8
FPR*	1.44	1.54	1.45	1.44	1.54	1.45
OPR*	40.5	50.2	42.3	40.5	50.2	42.3
T_{fuel} [K]	733	702	679	771	718	691
SFC [mg/Ns]	2.20	4.44	4.43	2.17	4.35	4.35
Δ SFC (relative to baseline)	−6.2 %	−3.7 %	−3.5 %	−7.7 %	−5.6 %	−5.3 %
EINOx [g/kg-fuel]	14.97	7.08	5.20	14.15	6.73	4.94
Δ EINOx (relative to baseline)	–33 %	−28 %	–23 %	−37 %	−31 %	−27 %

*Data kept constant

3.8. Conceptual design and impact on mission fuel burn

Conceptual design is carried out using the Chalmers in-house WEICO (WEIght and COst) tool. WEICO allows for an estimation of component-based weight and size of conventional turbomachinery. Additional weight models were developed for the heat exchangers.

The weight of the HEX is calculated based on the required number of tubes and fins, internal and external pressures, and material properties -

Table 15
Inlet and outlet temperatures and pressures for the recuperators in the intercooled-recuperated engines. The pressure variation on the air-side includes the loss in the connecting ducts.

OP	AR4			AR6		
	ToC (DP)	TO	Cruise	ToC (DP)	TO	Cruise
$T_{0,inlet,H2}$ [K]	336	350	311	344	366	327
$p_{0,inlet,H2}$ [MPa]	4.1918	4.1602	4.1968	4.1886	4.1387	4.1951
$T_{0,outlet,H2}$ [K]	702	733	679	718	771	691
$p_{0,outlet,H2}$ [MPa]	4.1672	4.0899	4.1786	4.1576	4.0517	4.1721
$T_{0,inlet,air}$ [K]	737	849	704	737	848	703
$p_{0,inlet,air}$ [MPa]	0.0434	0.1292	0.0382	0.0434	0.1291	0.0380
$T_{0,outlet,air}$ [K]	651	753	621	648	747	620
$p_{0,outlet,air}$ [MPa]	0.0357	0.1178	0.0321	0.0395	0.1233	0.0348

Aluminum 2219 for the intercoolers and Haynes 230 for the recuperators. The design specifications for the heat exchangers in the intercooled and intercooled-recuperated engines from Tables 13 and 14 are given in Table 16. It should also be noted that the used fin thickness is based on the fin geometry used by Kays [14] from which experimental heat transfer pressure data is available. The fin thickness corresponds to only 3.6 % of the fin spacing and could potentially be increased to match future requirements on strength, erosion, and possibly corrosion. A concept illustration of a heat exchanger with an area ratio of six is provided in Fig. 26.

Both the intercooler and recuperator heat exchangers can potentially have issues with icing. Recirculating pre-heated hydrogen can raise the surface temperature of the heat exchanger to avoid freezing, either continuously, or intermittently for de-icing, as was shown Section 3.1.2 of the paper. Compared to a (purely) recuperated engine, an intercooled-recuperated engine benefits from pre-heated hydrogen from the intercooler which can avoid icing in the water-rich exhaust of the recuperator, thereby only requiring recirculation in the intercooler. It bears mentioning that icing is a known challenge for cryogenic heat exchangers and is being actively researched elsewhere [82].

The conceptual designs of two intercooled-recuperated geared turbofan engines, featuring different heat exchanger area ratios are shown in Fig. 27. One can observe that the fan and nacelle sizes are retained across the different architectures and are equal to the one estimated for the baseline engine. An important difference can be readily identified in the high-pressure system, namely that the HPC stage count has decreased from 8 (baseline) to 6 with intercooling. This is due to the decrease in compression work due to precooling and reduced stage loading. However, it is important to note that the HPC last stage blade height across all designs is already quite a limiting factor. To alleviate this problem, it seems possible to slightly reduce the average radius of the HPC, however this will reduce the average blade speed and increase blade loading, possibly requiring an increase in stage count.

Table 16
Design specifications of the heat exchangers for the intercooled and intercooled-recuperated engine concepts.

	Intercooled AR4	Intercooled AR6	Intercooled-recuperated AR4		Intercooled-recuperated AR6	
	Interc.	Interc.	Interc.	Recup.	Interc.	Recup.
N_{tubes}	1656	1664	1674	2290	1681	2500
Tube dim. ($L_0 \times a$) [mm]	9.36 × 1.27	9.36 × 1.27	9.36 × 1.27	9.36 × 1.27	9.36 × 1.27	9.36 × 1.27
t_{tube} [mm]	0.508	0.508	0.508	0.508	0.508	0.508
N_{fins}	139	210	141	193	212	258
s_{fin} [mm]	1.4	1.4	1.4	1.4	1.4	1.4
δ_{fin} [μm]	50.8	50.8	50.8	50.8	50.8	50.8
L_y [m]	0.19	0.29	0.20	0.27	0.30	0.36
L_x [m]	0.08	0.08	0.08	0.08	0.08	0.08

Table 17 summarizes the conceptual design results for all the architectures, including the impact of the heat management system on engine weight and length. The impact on variation in mission fuel burn relative to the baseline is given in the last three columns and it is broken down into the contribution from SFC and engine weight variation. The impact of fan diameter on engine fuel burn is negligible and therefore not shown. It is noted that the intercooled AR4 concept seems to slightly reduce the engine weight. This is mainly caused by the increase in core specific power and decrease in HPC stages. The larger ducts and heat-exchanger sizes in the AR6 design leads to increased weight penalties, primarily in the recuperator due to the larger air volume in the exhaust. Still, the AR6 intercooled-recuperated design seems to provide a well-balanced design in terms of pressure loss and installation weight, capable of achieving a total mission fuel burn reduction of about 5.9 %.

4. Conclusions

This paper has presented results regarding the aerodynamic and engine system level performance for hydrogen-fueled aero engines featuring compact heat exchangers for intercooling and recuperation. A baseline turbofan engine has been designed for a short-to-medium range aircraft, which then served as the basis for the conceptual design of a compact heat exchanger for the purpose of intercooling. This resulted in two heat exchanger concepts, AR4 and AR6, with area ratios of 4 and 6 respectively, which achieved high effectiveness levels at the design point with low to moderate pressure drops. The AR6 heat exchanger achieved an effectiveness of 87 % compared to 80.2 % for the AR4 design. The air-side pressure drop amounted to 2.08 % for the AR4 design and 1.07 % for the AR6 design, which can be attributed to the lower HEX inlet velocities for the latter design.

A large aerodynamic optimization campaign was subsequently carried out which enabled the design of low loss diffuser ducts. It was found that the largest source of loss was due to the incidence of the flow relative to the heat exchanger fins, resulting in a near total loss of the kinetic energy of the velocity component perpendicular to the direction of the fins. For both designs this loss comprised roughly 60 % of all total pressure losses. In absolute terms the higher AR designs feature lower losses due to a lower dynamic pressure at the inlet of the heat exchanger. This is a clear area of improvement which should be achievable by either adjusting the incidence angle at the leading edge of the fins, employing curved fins, or using a larger duct with more diffusion.

System level studies of various engine configurations were then carried out using pressure drop correlations generated from the optimized duct geometries. Both intercooled and intercooled-recuperated engine concepts were investigated and compared to the baseline engine, retaining the same net thrust, OPR, and propulsive efficiency.

The final performance data was compared with the baseline engine not featuring any type of fuel pre-heating system. For intercooling it was found that SFC savings of 2.7–3.9 % were achieved when using an AR6 heat exchanger, depending on operating point. For the AR4 design the SFC savings ranged from 1.8 % to 2.7 %. NOx-emissions were decreased by up to 34 % at take-off for the AR6 design and 30 % for the AR4 design. The SFC savings were realized through pre-heating of the fuel in the intercooler and decreased compression work while NOx-emissions decreased due to lower combustor inlet temperatures.

For the AR4 intercooled-recuperated engine the SFC savings ranged from 3.5 % to 6.2 %, while the AR6 engine obtained larger SFC savings, ranging from 5.3 % at cruise to 7.7 % at take-off. This engine also featured the largest reduction in NOx-emissions, reaching 37 % at take-off conditions. The SFC savings for intercooled-recuperated engines stem from the elevated fuel temperatures after the recuperator, which are up to 400 K higher than the purely intercooled engine concepts.

Engine conceptual design highlighted two major differences relative to the baseline hydrogen engine; a decrease in the number of HPC stages due to decreased compression work associated with intercooling and increased weight due to the inclusion of the heat exchangers and ducts,

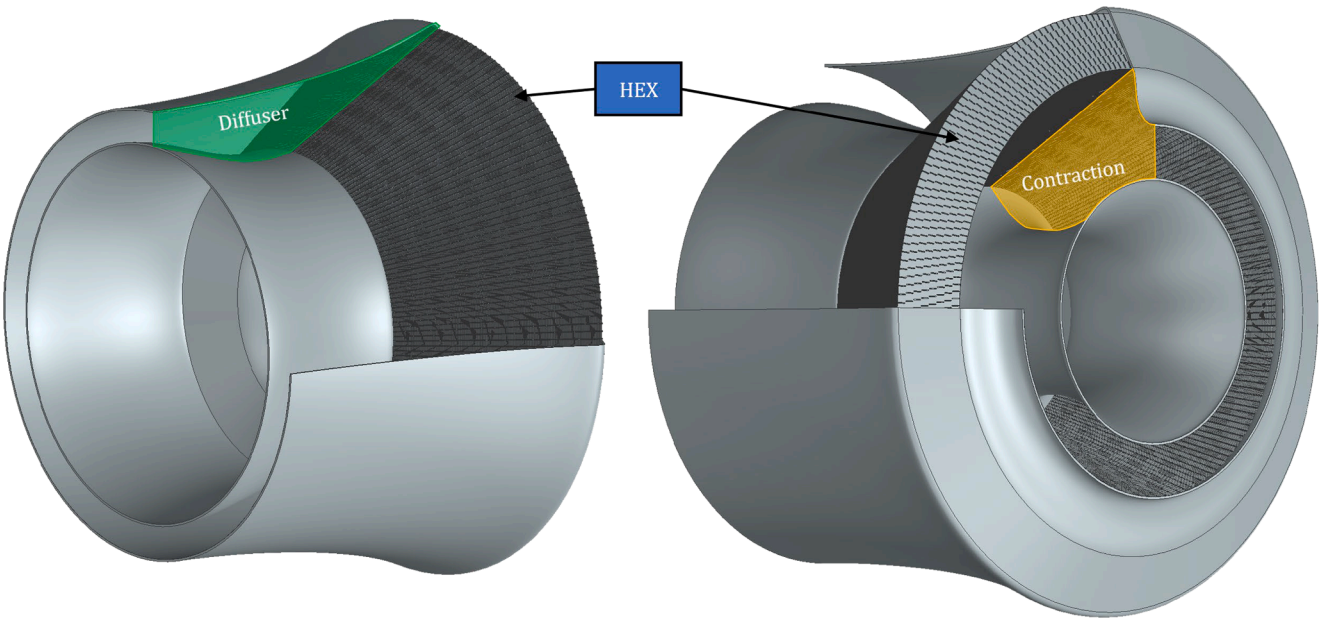

Fig. 26. Concept illustration for the AR 6 heat exchanger and connecting ducts. The image to the left shows where the core air flow from the LPC enters the diffuser, while the image to the right is where air. the contraction and enters the downstream HPC.

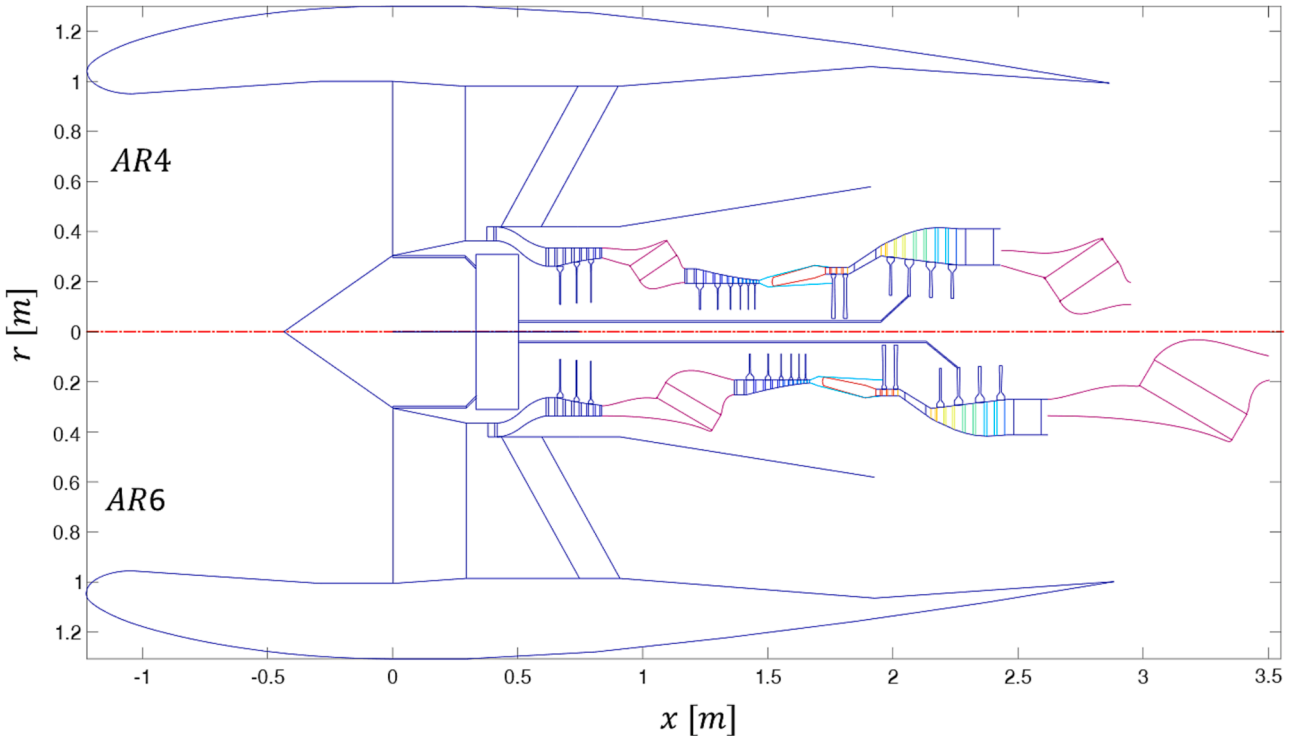

Fig. 27. Meridional cross-sectional drawing of the hydrogen intercooled geared turbofan engine.

Table 17
Engine properties and mission fuel burn for the different engine variants. Length is measured from fan leading edge to TRS trailing edge or recuperator exhaust.

	Mass [kg]	Architecture	HEX mass* [kg]	Length [m]	$\Delta_{FB,SFC}$	$\Delta_{FB,W}$	Δ_{FB}
Baseline	3392	1 + 3 + 8 + 2 + 4	–	2.46	datum	datum	datum
Interc. AR4	3354	1 + 3 + 6 + 2 + 4	70	2.41	−2.4 %	−0.15 %	−2.6 %
Interc. AR6	3402	1 + 3 + 6 + 2 + 4	129	2.6	−3.6 %	+0.04 %	−3.6 %
Interc. – Recup. AR4	3592	1 + 3 + 6 + 2 + 4	193	2.94	−4.5 %	+0.9 %	−3.7 %
Interc. – Recup. AR6	3681	1 + 3 + 6 + 2 + 4	326	3.5	−6.8 %	+1.4 %	−5.5 %

*HEX and ducts

especially for the recuperators. Nevertheless, the AR6 intercooled-recuperated engine achieved a fuel burn reduction of 5.5 % for the 3000 NM design mission.

These results highlight the excellent cooling capacity of hydrogen and how it can be used to improve both fuel consumption and NOx emissions on hydrogen-fueled aero engines. Further improvements in performance could be unlocked by re-optimizing the heat-exchanger cycles, which normally converge into an increased OPR, and decreasing the amount of turbine cooling air. Furthermore, the aero-thermal optimization of the heat exchanger matrix should be also investigated to fully explore the potential of hydrogen as a heat-sink with minimum pressure losses, added weight, and volume. Additional aspects that require further investigation are related to possible failure modes and mitigation paths. Safety issues are critical when introducing new engine technology, as it is expected that similar reliability levels will be achieved for production engines. When it comes to the introduction of hydrogen heat-exchangers in indirect contact with the hot parts of the engine, this poses a risk of leakage and hydrogen uncontained ignition within the compression system. One possible solution is the usage of a secondary fluid for heat-transfer in the core, hence eliminating the risk of hydrogen ignition. This would however increase the design complexity, decrease performance, and increase engine weight. Another safety aspect is related to ice formation and accumulation on the air side of the heat-exchanger in the presence of humid air, possibly leading to a partial or complete blockage of the core flow. This can be avoided by maintaining the air-side surface temperature above ice formation levels. This could be achieved by re-circulating the pre-heated hydrogen and subsequent mixing with the incoming cryogenic H2 as proposed in the present study. Another alternative could be to employ thermal cycling in the heat-exchanger to maintain a time-averaged surface temperature above water freezing levels. It should also be noted that, contrary to the intercooler, the recuperator always operates in humid gas conditions. Hence, the design of the recuperator in an intercooled-recuperated architecture would benefit from the hydrogen pre-heating in the intercooler, leading to a less stringent design than would otherwise be obtained for the isolated recuperator alternative.

CRediT authorship contribution statement

Alexandre Capitao Patrao: Writing – review & editing, Writing – original draft, Visualization, Methodology, Investigation, Conceptualization. **Isak Jonsson:** Writing - review and editing, Conceptualization. **Carlos Xisto:** Writing - review and editing, Methodology, Investigation, Supervision. **Anders Lundbladh:** Writing – review & editing. **Tomas Grönstedt:** Writing – review & editing, Methodology.

Declaration of Competing Interest

The authors declare that they have no known competing financial interests or personal relationships that could have appeared to influence the work reported in this paper.

Data availability

Data will be made available on request.

Acknowledgements

The work was financed and supported by Chalmers' Transport Area of Advance project "PATH - Pathways for a sustainable introduction of hydrogen into the aviation sector" and the Competence Centre TechForH2. The Competence Centre TechForH2 is hosted by Chalmers University of Technology and is financially supported by the Swedish Energy Agency (P2021-90268) and the member companies Volvo, Scania, Siemens Energy, GKN Aerospace, PowerCell, Oxeon, RISE, Stena Rederier AB, Johnsson Matthey and Insplorion. Support was also provided by the E.U. under the "ENABLEH2 – Enabling cryogenic hydrogen-based CO2 free air transport" project co-funded by the European Commission within the Horizon 2020 Programme (2014-2020) under Grant Agreement no. 769241. The simulations were enabled by resources provided by the National Academic Infrastructure for Supercomputing in Sweden (NAISS) and the Swedish National Infrastructure for Computing (SNIC) at C3SE partially funded by the Swedish Research Council through grant agreements no. 2022-06725 and no. 2018-05973.

References

[1] E. Commission, D.-G. for R. and Innovation, Fly the Green Deal – Europe's vision for sustainable aviation, Publications Office of the European Union, 2022. 10.2777/732726.
[2] European Commision, Communication From The Commission To The European Parliament, The European Council, The Council, The European Economic And Social Committee And The Committee Of The Regions-The European Green Deal., (2019) 1. https://eur-lex.europa.eu/legal-content/EN/TXT/?uri=COM:2019:640:FIN.
[3] European Commission, . Communication From The Commission To The European Parliament, The Council, The European Economic And Social Committee And The Committee Of The Regions "Fit For 55": Delivering The Eu's 2030 Climate Target On The Way To Climate Neutrality, (2021). https://eur-lex.europa.eu/legal-content/EN/TXT/?uri=COM:2021:550:FIN.
[4] E.J. Adler, J.R.R.A. Martins, Hydrogen-powered aircraft: fundamental concepts, key technologies, and environmental impacts, Fuel. 32 (2022) 7.
[5] N.C.W. Treleaven, S. Puggelli, R. Mercier, J. Leparoux, X. Sun, B. Sethi, High Altitude Relight Performance of Hydrogen-Air Micromix Combustion Systems, in: 2023: p. V03BT04A063. 10.1115/GT2023-103970.
[6] D. Abbot, A. Giannotta, X. Sun, P. Gauthier, V. Sethi, Thermoacoustic Behaviour of a Hydrogen Micromix Aviation Gas Turbine Combustor Under Typical Flight Conditions, in: 2021: p. V006T03A013. 10.1115/GT2021-59844.
[7] A. Edalatpour, A. Hassanvand, M.B. Gerdroodbary, R. Moradi, Y. Amini, Injection of multi hydrogen jets within cavity flameholder at supersonic flow, Int. J. Hydrogen Energy. 44 (2019) 13923–13931, https://doi.org/10.1016/j.ijhydene.2019.03.117.
[8] A. Anazadehsayed, M. Barzegar Gerdroodbary, Y. Amini, R. Moradi, Mixing augmentation of transverse hydrogen jet by injection of micro air jets in supersonic crossflow, Acta Astronaut. 137 (2017) 403–414, https://doi.org/10.1016/j.actaastro.2017.05.007.
[9] G.D. Brewer, Hydrogen Aircraft Technology (2017), https://doi.org/10.1201/9780203751480.
[10] D. Jian, Z. Qiuru, Key technologies for thermodynamic cycle of precooled engines: a review, Acta Astronaut. 177 (2020) 299–312, https://doi.org/10.1016/j.actaastro.2020.07.039.
[11] M. Coutinho, D. Bento, A. Souza, R. Cruz, F. Afonso, F. Lau, A. Suleman, F. R. Barbosa, R. Gandolfi, W. Affonso, F.I.K. Odaguil, M.F. Westin, R.J.N. dos Reis, C. R.I. da Silva, A review on the recent developments in thermal management systems for hybrid-electric aircraft, Appl. Therm. Eng. 227 (2023) 120427, https://doi.org/10.1016/j.applthermaleng.2023.120427.
[12] H. Abedi, C. Xisto, I. Jonsson, T. Grönstedt, A. Rolt, preliminary analysis of compression system integrated heat management concepts using LH2-based parametric gas turbine model, Aerospace. 9 (2022), https://doi.org/10.3390/aerospace9040216.
[13] J.J. Murray, A. Guha, A. Bond, Overview of the development of heat exchangers for use in air-breathing propulsion pre-coolers, Acta Astronaut. 41 (1997) 723–729, https://doi.org/10.1016/S0094-5765(97)00199-9.
[14] P. Dong, H. Tang, M. Chen, Study on multi-cycle coupling mechanism of hypersonic precooled combined cycle engine, Appl. Therm. Eng. 131 (2018) 497–506, https://doi.org/10.1016/j.applthermaleng.2017.12.002.
[15] I. Jonsson, C. Xisto, H. Abedi, T. Grönstedt, M. Lejon, Feasibility study of a radical vane-integrated heat exchanger for turbofan engine applications, in: Proc. ASME Turbo Expo, American Society of Mechanical Engineers, 2020: pp. 1–8. 10.1115/GT2020-15243.
[16] Y. Xu, H. Tang, M. Chen, F. Duan, Optimization and design of heat recovery system for aviation, Appl. Therm. Eng. 165 (2020) 114581, https://doi.org/10.1016/j.applthermaleng.2019.114581.
[17] X. Zhao, T. Grönstedt, Conceptual design of a two-pass cross-flow aeroengine intercooler, Proc. Inst. Mech. Eng. Part G J. Aerosp. Eng. 229 (2015) 2006–2023, https://doi.org/10.1177/0954410014563587.
[18] H. Canière, A. Willockx, E. Dick, M. De Paepe, Raising cycle efficiency by intercooling in air-cooled gas turbines, Appl. Therm. Eng. 26 (2006) 1780–1787, https://doi.org/10.1016/j.applthermaleng.2006.02.008.
[19] A. Capitao Patrao, I. Jonsson, C. Xisto, A. Lundbladh, M. Lejon, T. Grönstedt, The heat transfer potential of compressor vanes on a hydrogen fueled turbofan engine, Appl. Therm. Eng. 236 (2024) 121722, https://doi.org/10.1016/j.applthermaleng.2023.121722.
[20] F. Svensson, R. Singh, Effects of Using Hydrogen on Aero Gas Turbine Pollutant Emissions, Performance and Design, in: Vol. 2 Turbo Expo 2004, ASMEDC, 2004: pp. 107–116. 10.1115/GT2004-53349.

[21] F. Haglind, R. Singh, Design of aero gas turbines using hydrogen, J. Eng. Gas Turbines Power. 128 (2006) 754–764, https://doi.org/10.1115/1.2179468.
[22] V. Sethi, X. Sun, D. Nalianda, A. Rolt, P. Holborn, C. Wijesinghe, C. Xisto, I. Jonsson, T. Gronstedt, J. Ingram, A. Lundbladh, A. Isikveren, I. Williamson, T. Harrison, A. Yenokyan, Enabling cryogenic hydrogen-based CO 2 -free air transport: meeting the demands of zero carbon aviation, IEEE Electrif. Mag. 10 (2022) 69–81, https://doi.org/10.1109/MELE.2022.3165955.
[23] S. Boggia, A. Jackson, Some Unconventional Aero Gas Turbines Using Hydrogen Fuel, in: Turbo Expo 2002, Parts A B, ASMEDC, vol. 2, 2002, pp. 683–690. 10.1115/GT2002-30412.
[24] I.P. van Dijk, A.G. Rao, J.P. van Buijtene, Stator Cooling & Hydrogen Based Cycle, in: International Symposium on Air Breathing Engines 2009, Montreal, 2009.
[25] F. Yin, A. Gangoli Rao, A. Bhat, M. Chen, Performance assessment of a multi-fuel hybrid engine for future aircraft, Aerosp. Sci. Technol. 77 (2018) 217–227, https://doi.org/10.1016/j.ast.2018.03.005.
[26] P. Liu, H. Han, Z. Bao, Multi-objective optimization of fuel–air tube-in-tube helical coil heat exchangers for cooled cooling air system applied in aeroengines, Aerosp. Sci. Technol. 130 (2022) 107933, https://doi.org/10.1016/j.ast.2022.107933.
[27] D. Missirlis, K. Yakinthos, A. Palikaras, K. Katheder, A. Goulas, Experimental and numerical investigation of the flow field through a heat exchanger for aero-engine applications, Int. J. Heat Fluid Flow. 26 (2005) 440–458, https://doi.org/10.1016/j.ijheatfluidflow.2004.10.003.
[28] K. Yakinthos, D. Missirlis, A. Palikaras, P. Storm, B. Simon, A. Goulas, Optimization of the design of recuperative heat exchangers in the exhaust nozzle of an aero engine, Appl. Math. Model. 31 (2007) 2524–2541, https://doi.org/10.1016/j.apm.2006.10.008.
[29] D. Misirlis, Z. Vlahostergios, M. Flouros, C. Salpingidou, S. Donnerhack, A. Goulas, K. Yakinthos, Optimization of heat exchangers for intercooled recuperated Aero Engines, Aerospace. 4 (2017), https://doi.org/10.3390/aerospace4010014.
[30] C. Zhang, V. Gümmer, The potential of helicopter turboshaft engines incorporating highly effective recuperators under various flight conditions, Aerosp. Sci. Technol. 88 (2019) 84–94, https://doi.org/10.1016/j.ast.2019.03.008.
[31] V. Kumar Cheeda, R.V. Kumar, G. Nagarajan, Design and CFD analysis of a regenerator for a turboshaft helicopter engine, Aerosp. Sci. Technol. 12 (2008) 524–534, https://doi.org/10.1016/j.ast.2007.12.005.
[32] Y. Ito, T. Nagasaki, Suggestion of Intercooled and Recuperated Jet Engine Using Already Equipped Components as Heat Exchangers, in: 47th AIAA/ASME/SAE/ASEE Jt. Propuls. Conf. & Exhib., American Institute of Aeronautics and Astronautics, Reston, Virigina, 2011: pp. 1–16. 10.2514/6.2011-6102.
[33] X. Zhao, M. Tokarev, E. Adi Hartono, V. Chernoray, T. Grönstedt, Experimental validation of the aerodynamic characteristics of an aero-engine intercooler, J. Eng. Gas Turbines Power. 139 (2016), https://doi.org/10.1115/1.4034964.
[34] X. Zhao, O. Thulin, T. Grönstedt, First and second law analysis of intercooled turbofan engine, J. Eng. Gas Turbines Power. 138 (2015), https://doi.org/10.1115/1.4031316.
[35] A.M. Rolt, K.G. Kyprianidis, Assessment of new aeroengine core concepts and technologies in the EU framework 6 NEWAC programme, 27th Congr. Int. Counc. Aeronaut. Sci. 2010, ICAS 2010. 4 (2010) 2736–2746.
[36] L. Xu, K.G. Kyprianidis, T.U.J. Grönstedt, Optimization study of an intercooled recuperated aero-engine, J. Propuls. Power. 29 (2013) 424–432, https://doi.org/10.2514/1.B34594.
[37] L. Xu, T. Grönstedt, Design and analysis of an intercooled turbofan engine, J. Eng. Gas Turbines Power. 132 (2010), https://doi.org/10.1115/1.4000857.
[38] D.G. Wilson, The Design of High-Efficiency Turbomachinery and Gas Turbines, 2014.
[39] H. Grieb, Projektierung von Turboflugtriebwerken, Birkhäuser Basel, Basel (2004), https://doi.org/10.1007/978-3-0348-7938-5.
[40] J. Kurzke, I. Halliwell, Propulsion and power, springer international publishing, Cham (2018), https://doi.org/10.1007/978-3-319-75979-1.
[41] W.M. Kays, A.L. London, Compact Heat Exchangers, second ed., McGraw-Hill, 1984.
[42] F.P. Incropera, D.P. DeWitt, T.L. Bergman, A.S. Lavine, Fundamentals of Heat and Mass Transfer, 6th ed., Wiley, New York, 2007.
[43] B.S. Petukhov, J.P. Hartnett, T.F. Irvine, Advances in Heat Transfer Vol. 6, 1970.
[44] V. Gnielinski, New equations for heat and mass transfer in turbulent pipe and channel flow, Int. Chem. Eng. 16 (1976) 359–368. https://api.semanticscholar.org/CorpusID:136639967.
[45] E.W. Lemmon, I.H. Bell, M. Huber, M. McLinden, NIST standard reference database 23: reference fluid thermodynamic and transport properties - REFPROP, Version 10 (2018).
[46] I.H. Bell, J. Wronski, S. Quoilin, V. Lemort, Pure and pseudo-pure fluid thermophysical property evaluation and the open-source thermophysical property library coolprop, Ind. Eng. Chem. Res. 53 (2014) 2498–2508, https://doi.org/10.1021/ie4033999.
[47] J.W. Leachman, R.T. Jacobsen, S.G. Penoncello, E.W. Lemmon, Fundamental equations of state for parahydrogen, normal hydrogen, and orthohydrogen, J. Phys. Chem. Ref. Data. 38 (2009) 721–748, https://doi.org/10.1063/1.3160306.
[48] J. Natterer, J. Bargon, Parahydrogen induced polarization, Prog. Nucl. Magn. Reson. Spectrosc. 31 (1997) 293–315, https://doi.org/10.1016/S0079-6565(97)00007-1.
[49] E. Karlsson, Catalytic ortho- to Para-Hydrogen Conversion in Liquid Hydrogen, Lund Univ, Sweden, 2017, p. 100.
[50] D.H. Weitzel, W. Loebenstein, J.W. Draper, O.E. Park, Ortho-para catalysis in liquid-hydrogen production, J. Res. Natl. Bur. Stand. 60 (1958) (1934) 221–227.
[51] S. Wagner, Conversion rate of para-hydrogen to ortho-hydrogen by oxygen: Implications for PHIP gas storage and utilization, Magn. Reson. Mater. Physics, Biol. Med. 27 (2014) 195–199, https://doi.org/10.1007/s10334-013-0399-y.
[52] G. Montero Villar, D. Lindblad, N. Andersson, Effect of airfoil parametrization on the optimization of counter rotating open rotors, in: AIAA Scitech 2019 Forum, American Institute of Aeronautics and Astronautics, 2019, https://doi.org/10.2514/6.2019-0698.
[53] G. Montero Villar, D. Lindblad, N. Andersson, Multi-Objective Optimization of an Counter Rotating Open Rotor using Evolutionary Algorithms, in: 2018 Multidiscip. Anal. Optim. Conf., American Institute of Aeronautics and Astronautics, 2018. doi: 10.2514/6.2018-2929.
[54] A. Capitao Patrao, G. Montero Villar, J. Takachi Tomita, C. Bringhenti, R. Avellan, A. Lundbladh, T. Grönstedt, An optimization platform for high speed propellers, in: Aerosp. Technol. Congr. 2016, 2016.
[55] M.M. Aslam Bhutta, N. Hayat, M.H. Bashir, A.R. Khan, K.N. Ahmad, S. Khan, CFD applications in various heat exchangers design: a review, Appl. Therm. Eng. 32 (2012) 1–12, https://doi.org/10.1016/j.applthermaleng.2011.09.001.
[56] D.J. Cerantola, A.M. Birk, Experimental validation of numerically optimized short annular diffusers, J. Eng. Gas Turbines Power. 137 (2015) 1–10, https://doi.org/10.1115/1.4028679.
[57] ANSYS Inc., ANSYS Fluent, User's Guide 2021 (2021) R1.
[58] P. Virtanen, R. Gommers, T.E. Oliphant, M. Haberland, T. Reddy, D. Cournapeau, E. Burovski, P. Peterson, W. Weckesser, J. Bright, S.J. van der Walt, M. Brett, J. Wilson, K.J. Millman, N. Mayorov, A.R.J. Nelson, E. Jones, R. Kern, E. Larson, C. J. Carey, Y. \.Ilhan Polat, E.W. Feng, J. Moore, D. VanderPlas, J. Laxalde, R. Perktold, I. Cimrman, E.A. Henriksen, C.R. Quintero, A.M. Harris, A. H. Archibald, F. Ribeiro, P. van Pedregosa, Mulbregt, SciPy 1.0 contributors, SciPy 1.0: fundamental algorithms for scientific computing in python, Nat. Methods. 17 (2020) 261–272, https://doi.org/10.1038/s41592-019-0686-2.
[59] K. Deb, A. Pratap, S. Agarwal, T. Meyarivan, A fast and elitist multiobjective genetic algorithm: NSGA-II, IEEE Trans. Evol. Comput. 6 (2002) 182–197, https://doi.org/10.1109/4235.996017.
[60] D.S. Kumar, K.L. Kumar, Effect of swirl on pressure recovery in annular diffusers, J. Mech. Eng. Sci. 22 (1980) 305–313, https://doi.org/10.1243/JMES_JOUR_1980_022_056_02.
[61] T. Grönstedt, Development of Methods for Analysis and Optimization of Complex Jet Engine Systems, Chalmers University of Technology, 2000.
[62] T. Grönstedt, M. Irannezhad, X. Lei, O. Thulin, A. Lundbladh, First and second law analysis of future aircraft engines, J. Eng. Gas Turbines Power. 136 (2014), https://doi.org/10.1115/1.4025727.
[63] T. Grönstedt, M. Wallin, A comparative study of genetic algorithms and gradient methods for RM12 turbofan engine diagnostics and performance estimation, in: Turbo Expo 2004, ASMEDC, vol. 2, 2004, pp. 615–624. 10.1115/GT2004-53591.
[64] O. Thulin, O. Petit, C. Xisto, X. Zhao, T. Grönstedt, First and second law analysis of radical intercooling concepts, J. Eng. Gas Turbines Power. 140 (2018), https://doi.org/10.1115/1.4038364.
[65] C. Xisto, O. Petit, T. Grönstedt, A. Lundbladh, Assessment of CO2 and NOx emissions in intercooled pulsed detonation turbofan engines, J. Eng. Gas Turbines Power. 141 (2019), https://doi.org/10.1115/1.4040741.
[66] G. Sanford, B.J. McBride, Computer Program for Calculation of Complex Chemical Equilibrium Compositions and Applications. NASA Reference Publication, 1311, Cleveland, Ohio, 1994.
[67] A. Rolt, V. Sethi, F. Jacob, J. Sebastiampillai, C. Xisto, T. Grönstedt, L. Raffaelli, Scale effects on conventional and intercooled turbofan engine performance, Aeronaut. J. 121 (2017) 1162–1185, https://doi.org/10.1017/aer.2017.38.
[68] A. Capitao Patrao, C. Xisto, I. Jonsson, A. Lundbladh, D2.4 – Final report on heat management system, 2023. https://ec.europa.eu/research/participants/documents/downloadPublic?documentIds=080166e5f6b47829&appId=PPGMS.
[69] C. Xisto, A. Lundbladh, Design and Performance of Liquid Hydrogen Fuelled Aircraft for Year 2050 EIS, in: 33rd Congr. Int. Counc. Aeronaut. Sci. ICAS 2022, 2022: pp. 1119–1131.
[70] I. Jonsson, Experimental aerothermal study of internal jet engine structure, Chalmers University of Technology (2021). https://research.chalmers.se/en/publication/527645.
[71] C.O. Dueñas, R.J. Miller, H.P. Hodson, J.P. Longley,PART A, Effect of length on compressor inter-stage duct performance, Proc. ASME Turbo Expo. 6 (2007) 319–329, https://doi.org/10.1115/GT2007-27752.
[72] J.V. Taylor, F. Flanagan, A. Dunlop, S.D. Grimshaw, R.J. Miller, Super aggressive S-ducts for air breathing rocket engines, J. Turbomach. 143 (2021), https://doi.org/10.1115/1.4050596.
[73] E.D. Marquardt, J.. Le, R. Radebaugh, Cryogenic Material Properties Database, in: 11th Int. Cryocooler Conf. June 20-22, Keystone, 2000.
[74] NIST, Material Properties: 5083 Aluminum (UNS A95083), (n.d.). https://trc.nist.gov/cryogenics/materials/5083 Aluminum/5083Aluminum_rev.htm (Accessed November 20, 2023).
[75] N.J. Simon, E.S. Drexler, R.P. Reed, Review of Cryogenic Mechanical and Thermal Properties of Al-Li Alloys and Alloy 2219 (1990) 1–183.
[76] R.M. Davis, Space Shuttle External Tank Project Status, in: Sp. Congr. Proc. 4, 1980.
[77] A. Gomez, H. Smith, Liquid hydrogen fuel tanks for commercial aviation: Structural sizing and stress analysis, Aerosp. Sci. Technol. 95 (2019) 105438, https://doi.org/10.1016/j.ast.2019.105438.
[78] AZoM, Aluminium / Aluminum 7050 Alloy (UNS A97050), (2012). Aluminium / Aluminum 7050 Alloy (UNS A97050) (accessed November 17, 2023).
[79] D.S. Miller, Internal Flow Systems, 2nd ed., BHRA (Information Services), 1990.

[80] Haynes International, Haynes 230 alloy - Principal Features, 2021. https://www.haynesintl.com/docs/default-source/pdfs/new-alloy-brochures/high-temperature-alloys/brochures/230-brochure.pdf.
[81] J. Tacconi, N. Grech, Advanced Hydrogen Cycles to Help Decarbonize the Aviation Industry. Part 1: Development of Simulation & Modeling Toolsets, in: Vol. 1 Aircr. Engine, American Society of Mechanical Engineers, 2023. 10.1115/GT2023-103505.
[82] R. Varvill, Heat exchanger development at Reaction Engines Ltd, Acta Astronaut. 66 (2010) 1468–1474, https://doi.org/10.1016/j.actaastro.2009.11.010.